CHALMERS
UNIVERSITY OF TECHNOLOGY

Reconstruction of sleeper displacements from measured accelerations for model-based condition monitoring of railway crossing panels

Citation for the original published paper (version of record):
Milosevic, M., Pålsson, B., Nissen, A. et al (2023). Reconstruction of sleeper displacements from measured accelerations for model-based condition
monitoring of railway crossing panels. Mechanical Systems and Signal Processing, 192.
http://dx.doi.org/10.1016/j.ymssp.2023.110225

(article starts on next page)

Mechanical Systems and Signal Processing 192 (2023) 110225

Contents lists available at ScienceDirect

Mechanical Systems and Signal Processing

journal homepage: www.elsevier.com/locate/ymssp

Reconstruction of sleeper displacements from measured accelerations for model-based condition monitoring of railway crossing panels

Marko D.G. Milošević [a,*], Björn A. Pålsson [a], Arne Nissen [b], Jens C.O. Nielsen [a], Håkan Johansson [a]

[a] *Chalmers University of Technology, Department of Mechanics and Maritime Sciences, 412 96 Göteborg, Sweden*
[b] *The Swedish Transport Administration, Box 809, 971 25 Luleå, Sweden*

ARTICLE INFO

Keywords:
Displacement double integration
Wireless accelerometer sensor
Condition monitoring
Railway crossing
3D scan
Multibody simulations

ABSTRACT

Railway switches and crossings (S&C, turnouts) connect different track sections and create a railway network by allowing trains to change tracks. This functionality comes at a cost as the load-inducing rail discontinuities in the switch and crossing panels cause much larger degradation rates for S&C compared to regular plain line tracks. The high degradation rates make remote condition monitoring an interesting prospect for infrastructure managers to optimise maintenance and ensure safe operations. To this end, this paper addresses the development of tailored signal processing tools for condition monitoring using embedded accelerometers in crossing panels. Multibody simulations of the dynamic train–track interaction are used to aid the interpretation of the measured signals in a first step towards building a model-based condition monitoring system. An analysis is performed using sleeper acceleration measurement data generated by 100 000 train passages in eight crossing panels. Based on the given data, a novel frequency-domain displacement reconstruction method is developed and the robustness of the method with respect to encountered operational variability of the measured data is demonstrated. The separation of the track response into quasi-static and dynamic domains based on deformation wavelength regions is proposed as a promising strategy to observe the ballast condition and the crossing geometry condition, respectively.

1. Introduction

In a railway network, the components that allow for trains to switch from one track to another are called switches & crossings (S&C's, turnout). The subject of this paper is a standard S&C with a fixed crossing and its layout is presented in Fig. 1. In the switch panel, there are flexible switch rails that are actuated with switching machines to guide trains into the through or diverging routes. In the crossing panel, the arrangement of rails includes a crossing nose and two wing rails that allow for wheels to travel across the two intersecting routes. Further, there are check rails that impose a lateral constraint on passing wheelsets to prevent excessive lateral movement and derailment during the crossing transition. Traffic in the facing direction (move) goes from the switch panel towards the crossing panel, while traffic in the trailing move goes in the opposite direction.

---

* Corresponding author.
E-mail address: marko.milosevic@chalmers.se (M.D.G. Milošević).

https://doi.org/10.1016/j.ymssp.2023.110225
Received 5 July 2021; Received in revised form 4 February 2023; Accepted 17 February 2023

The functionality of switching trains between tracks comes at a cost, however, as the rail discontinuities in the switch and crossing panels induce high magnitudes of wheel–rail contact forces that make S&C subjected to much higher degradation rates compared to regular plain line tracks. Examples of degradation include damage to the running surface of the crossing nose and wing rails due to wear, plastic deformation, rolling contact fatigue, and deterioration of sleeper support conditions and track geometry due to settlement of ballast and subgrade. For a study on observed failures in S&C see [2]. The high degradation rates of S&C are the reason why railway infrastructure managers spend from tens to hundreds of millions of Euros annually on their maintenance. In Sweden, the annual maintenance cost for around 12 000 S&C is estimated to be 400 – 450 MSEK (~40 – 45 MEUR) [3]. In the United Kingdom, the corresponding cost in 2012 for around 20 000 S&C was 189 MGBP (~212 MEUR), with an additional cost of 220 MGBP (~246 MEUR) for renewals [4]. For comparison, Germany has 69 983 (2014) S&Cs [4], France 25 600, and Switzerland 15 062 (2009) [5].

The high cost for S&C maintenance creates a potential business case for systems that can allow for improved maintenance decisions compared to what can be achieved from periodic inspection intervals using measurement vehicles or visual inspection by engineers in track. One such candidate system is an online condition monitoring system that provides a continuous diagnosis of the structural response of an S&C via the processing of signals from embedded sensors. To this end, this study presents a set of signal processing tools developed to analyse the track response from measured accelerations under traffic loading. The developments target the monitoring of ballast settlement and crossing geometry degradation which are key degradation modes in crossing panels [2,6,7]. Ballast settlement will reduce the support stiffness of the track and therefore increase the quasi-static track displacement [8] while a degraded crossing geometry corresponds to an increased dip irregularity in the rail that will increase the dynamic excitation of the track under passing wheels [9]. The present investigations are formed around an existing concept for crossing panel instrumentation using an accelerometer permanently mounted on top of the sleeper at the crossing transition, see Fig. 2(a). The sensors are provided by Konux GmbH and are installed in the Swedish railway network as a part of Trafikverket's (the Swedish Railway Administration) research activities on remote condition monitoring of crossing panels initiated in the EU-funded In2Rail project [10]. Data from eight different crossing panels and a total of 100 000 train passages recorded over 110 days has been analysed. The main developments presented in the paper are:

1) A novel method for sleeper displacement reconstruction from measured accelerations. The method is based on integration in the frequency domain using optimised parameters for baseline and low-frequency filtering and is developed for automatised processing of long-term remote condition monitoring data. A key objective in the development of this method has therefore been robustness for processing of signals from different turnouts and traffic conditions to provide a foundation for reliable condition monitoring.
2) A proposed decomposition of the reconstructed sleeper displacement signals into quasi-static and dynamic frequency domains to observe the ballast and crossing geometry conditions, respectively.
3) A method for train type and speed identification based on the cross-correlation of filtered acceleration signals. The method is developed to enable a direct comparison of the measured responses between crossing panels stemming from the same train type and speed, thus reducing the uncertainty in measurements due to variability in operational conditions. The presented results are from passages of identified X2 high-speed and X31 regional passenger trains.

Additionally, to interpret the measured responses, simulations of dynamic vehicle–track interaction are performed for a number of track parameter variations including different ballast support conditions and measured crossing rail geometries from in situ crossings. Related papers such as [9,11,12] have contrasted measured accelerations at the crossing transition to simulation results, but their focus is on model validation or the study of a particular phenomenon such as sound radiation from the crossing impact rather than analysis of the displacement response for condition monitoring.

The presented developments are part of a larger effort to develop a model-based numerical procedure that can not only identify but also predict the structural condition of S&C via embedded sensors. The target system can be described as a Digital Twin representation of the physical system where simulation models, condition monitoring data, and maintenance history are combined to predict and identify the maintenance needs for S&C. See also [13] for a broader overview of condition monitoring and instrumentation techniques in S&C.

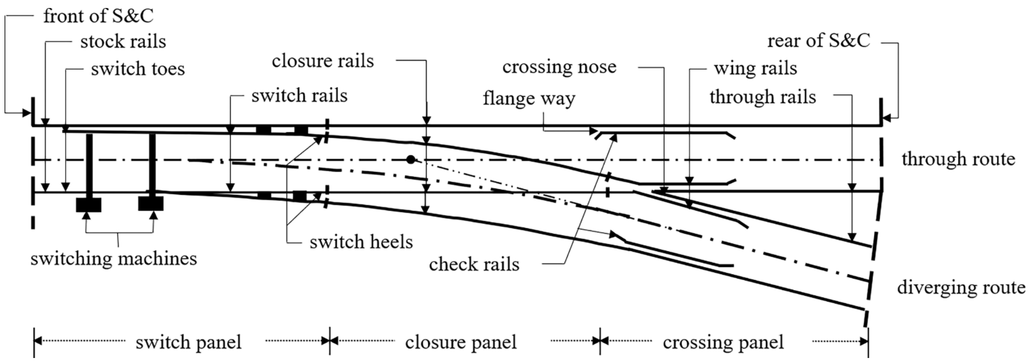

Fig. 1. Layout, components, and nomenclature for a standard right-hand side S&C with a fixed crossing [1].

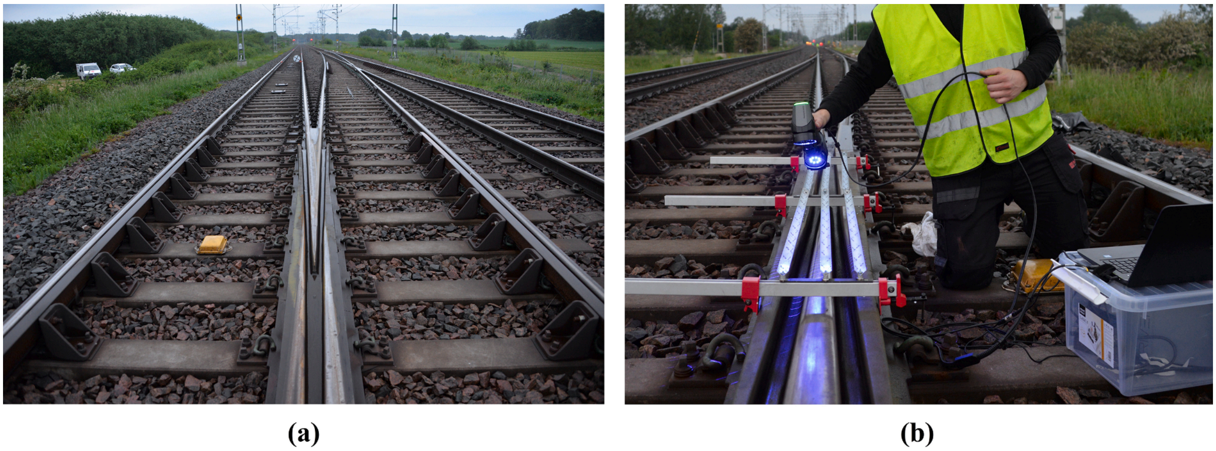

Fig. 2. (a) Accelerometer from Konux GmbH (yellow box) installed on the sleeper adjacent to the crossing transition. (b) 3D geometry scan of a crossing transition. (For interpretation of the references to colour in this figure legend, the reader is referred to the web version of this article.)

2. Instrumentation and field data

The studies in this paper are based on two types of measurement data. The first is acceleration recordings obtained with permanently installed accelerometers, see Fig. 2a, and they constitute the cornerstone for the developments in this paper. The second is in-situ 3D geometry scans of crossing rails, see Fig. 2b, which are used to simulate dynamic vehicle-S&C interaction. Both the acceleration recordings and crossing geometry scans were taken from the same locations on the southern main line in Sweden named after the adjacent villages Höör and Stehag. The acceleration measurements were performed between September 2017 and January 2018, while the 3D scans were performed in June 2019. Crossing panels with acceleration measurements are referred to as Höör with network IDs [21A, 21B, 22A, 22B] and Stehag with IDs [21A, 21B, 31A, 32B]. Although the scanned crossings come from Höör 22A and Stehag 21A, as the geometry scans and acceleration measurements are not concurrent in time no direct link is established between accelerations and scanned crossing geometries, and the scanned crossings are referred to as crossing A and crossing B. The geometry scans are used only for qualitative comparisons in simulations.

2.1. *Acceleration data*

The accelerometer is placed on the sleeper adjacent to the crossing transition at a position that is centred between the two rails in the through route. The acceleration recordings cover around 100 000 train passages divided between the eight crossing panels at Höör and Stehag. Details of the acceleration recordings and each turnout are given in Table 1. The turnout designs differ between the two locations. In Höör, the latest generation of turnouts (EV-60E) is installed featuring rail fastenings with a soft resilient element (rail pad) between the crossing rail and sleepers. Stehag features an older design (UIC60) with a direct and very stiff connection between the crossing rail and sleepers. In addition to the variation in turnout design, there are also variations in radius and predominant traffic direction. One example of acceleration recording is shown in Fig. 3, where 22 axle passages are observed as the local maxima in the signal.

The accelerometer is activated by track vibrations from oncoming trains and is not measuring between train passages. The recorded signals, therefore, include a non-physical wake-up transient at the beginning of the recording. The wake-up setting was not sensitive enough at the time of measurement causing this transient to interfere with the signal part corresponding to the locomotive axels. In these instances, the corrupted part of the signal was discarded. Additionally, if the signal reaches the measurement limit of ±50 g, it is considered corrupted and is discarded from the data set. Signals with a maximum acceleration magnitude lower than 1 g are also

Table 1
Summary of acceleration recordings for eight crossing panels acquired during the period 2017-09-28 – 2018-01-24.

Experimental data and monitoring location information								
Location	Höör	Höör	Höör	Höör	Stehag	Stehag	Stehag	Stehag
Crossing name	21A	21B	22A	22B	21A	21B	31A	32B
Design	EV-60E 1:18.5	EV-60E 1:18.5	EV-60E 1:18.5	EV-60E 1:18.5	UIC60 1:18.5	UIC60 1:18.5	UIC60 1:15	UIC60 1:15
Direction	Trailing	Trailing	Facing	Facing	Facing	Facing	Trailing	Facing
Radius	1200 m	1200 m	1200 m	1200 m	1200 m	1200 m	760 m	760 m
# of train passages	12,243	11,854	13,974	11,281	13,024	14,022	12,813	12,738
# of train passages 1 g $<$ acceleration $<$ 50 g	11,626	10,918	13,146	10,940	9022	7203	10,549	6519
# of X2 and X31 train passages	2532	3136	2576	2160	1236	619	2329	250

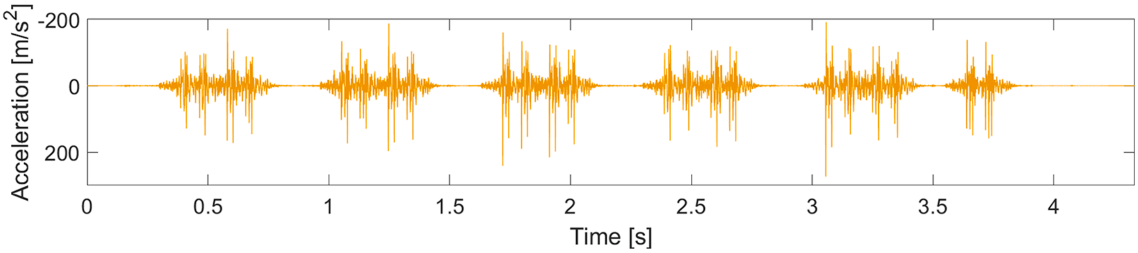

Fig. 3. Example of sleeper acceleration recording, positive acceleration direction is downwards into the track.

discarded. In Table 1, it is shown that the crossing panels Stehag 21B and 32B have a lower number of identified X2 and X31 passenger trains and a higher number of discarded signals. For these two crossings, it was concluded that the significant number of discarded X2 and X31 passenger trains was due to accelerations exceeding 50 g. The properties of the accelerometer are given in Table 2. The methods developed in this paper are based on raw data coming directly from the sensor without any pre-processing. Fig. 4 shows peak magnitudes of acceleration recordings for the eight crossing panels and 110 days of monitoring. It can be observed that crossings undergo large operational variability and that the older turnout design in Stehag (UIC60) with stiffer connections between rail and sleeper has higher acceleration levels.

2.2. *Geometry data*

The crossing rail geometry was obtained using the high-precision Creaform HandySCAN 3D laser scanner, see Fig. 2(b). During in situ scanning, additional reference objects were mounted on the crossing rail to increase the quality of the scan. The properties of the scanner are given in Table 3. Two scanned and post-processed crossing rail geometries are shown in Fig. 5 and Fig. 6. These crossing rail geometries were chosen as they represent two different states of degradation of the running surface. The geometry of crossing A (Fig. 5) shows very few signs of geometry change from the nominal design, while crossing B (Fig. 6) shows intermediate wear.

3. Model for simulation of train-track interaction

To improve the understanding of the measured data, the dynamic vehicle–track interaction in the crossing panel is modelled and simulated using multi-body simulations (MBS). The analyses are performed with the commercial software Simpack (v.2019). A 3D view of the model is presented in Fig. 7. The track model is a finite element model with all the rails and sleepers described by Timoshenko beam elements that are condensed to the so-called super elements using the Craig-Bampton method [14]. The condensation reduces the size of the underlying finite element model, but primarily the method was used as this is the input format required for flexible track structures in Simpack. The node spacing of the super elements is presented in Table 4, and the node spacing in the original FE model is half of that. The crossing is at the longitudinal centre of the track model. Each sleeper is supported by a discretised system of independent bushings (springs and viscous dampers) in the vertical direction that represent the ballast (Winkler bed). Each connection between the sleeper and rail is modelled by a single bushing element representing the rail fastening. The nodes of the rails and sleepers are partially constrained to reduce model size. Here, the sleeper nodes can displace vertically, while the rail nodes can displace vertically and laterally. In total, the number of degrees of freedom of the track model is 2026. The model is generated with an S&C model generation script [10] and implemented in Simpack using its non-linear flextrack functionality. Additionally, see [15] for a thorough evaluation of numerical approaches for simulating train–track interactions for S&C.

A convergence study has been performed concerning the required length of the track model to save computational effort while maintaining accuracy. The study started with a track model of 100 sleepers in length. For different lengths of the model, sleeper, and rail accelerations were compared in the region ±6 m from the crossing transition. For the present investigation, it was found that a track model of 21.6 m in length (37 sleepers) is sufficient for simulating the 12 m (±6 m) of single train bogie passage over the crossing transition (in facing and trailing moves). The vehicle is modelled as a single bogie according to the passenger vehicle model from the Manchester benchmarks study [16], but with adjusted mass properties to correspond to the axle loads of the X2 train cab car bogie (15.5 tonnes). The input to the MBS model is presented in Table 4. The crossing rail geometry in the simulations is represented by 2D profiles discretised from the 3D scans of the crossing rail, see Fig. 9, or from a nominal generic crossing from the S&C benchmark study

Table 2
Konux GmbH accelerometer properties.

Sensor information	
Device	Monoaxial cellular accelerometer
Installation	Permanent sleeper connection
Direction of measurements	Vertical
Sampling rate	20 kHz
Range	±50 g

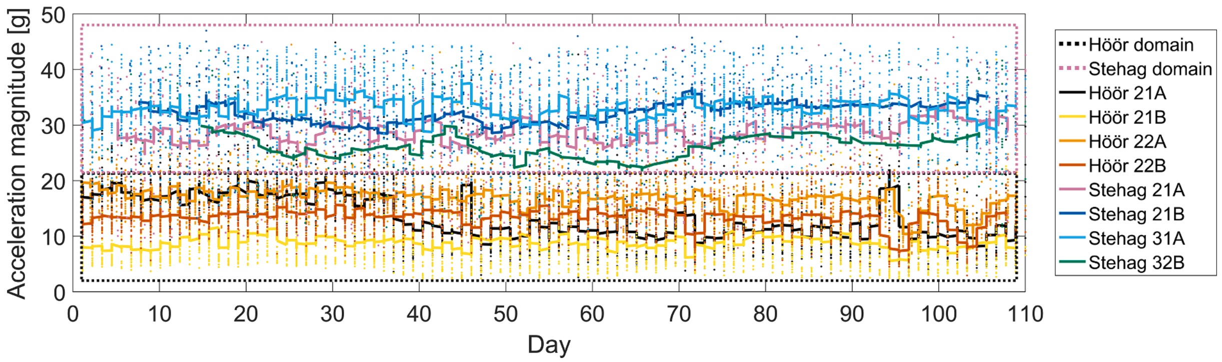

Fig. 4. Peak magnitudes of train acceleration recordings for the eight crossing panels and 110 days of monitoring. Scatter points represent single train passage of X2 and X31 trains, and continuous lines represent 25 points moving-average filter of the scatter points for each crossing panel.

Table 3
Creaform HandySCAN 3D scanner properties.

Scanner information	
Device	Portable 3D laser scanner
Accuracy	0.035 mm
Measurement resolution	0.025 mm
Mesh resolution	0.1 mm
Measurement rate	800 000 measurements/s
Light source	7 laser crosses
Scanning area	310 × 350 mm

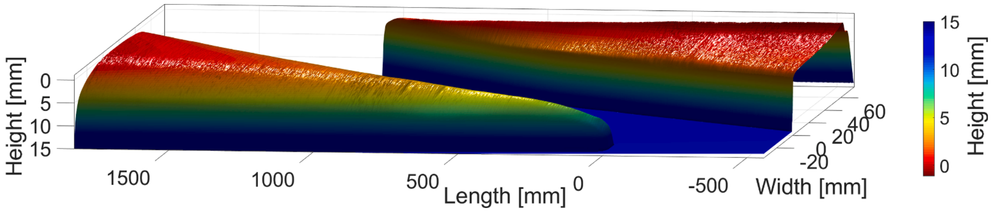

Fig. 5. Crossing A: 3D scan of crossing nose (left) and wing rail (right).

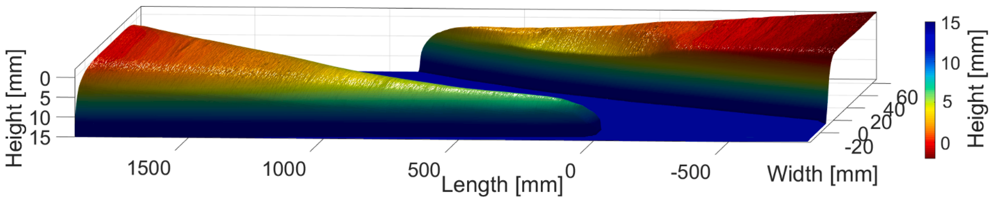

Fig. 6. Crossing B: 3D scan of crossing nose (left) and wing rail (right).

[17] that is used here as a reference case. The software builds a 3D rail geometry from the 2D sections via a cubic spline interpolation. A 10 mm longitudinal profile spacing is used in the transition area between the crossing nose and wing rail. An equivalent linearised Hertz contact is used for the normal wheel–rail contact, while FASTSIM [18] is used to model the tangential contact. A 2D cross-section of the vehicle–track model is shown in Fig. 8. The train speed is 160 km/h and the simulations start from a static equilibrium position for the vehicle–track system.

The MBS model is used in a study of five cases representing different combinations of crossing rail geometry, rail pad properties, and linear or nonlinear ballast properties, see Table 5. Supported by the results presented in Milne et al. [19], railway track properties can encounter a significant variation along its length, primarily due to irregularities in the support conditions. In this paper, the investigations are made to study the influence of different track properties on the dynamic response of the crossing as measured by the accelerometer. A bi-linear stiffness function is used to model the nonlinear ballast properties that occur at a voided sleeper. The function has zero stiffness in the void region and a linear stiffness from the point where the void is closed.

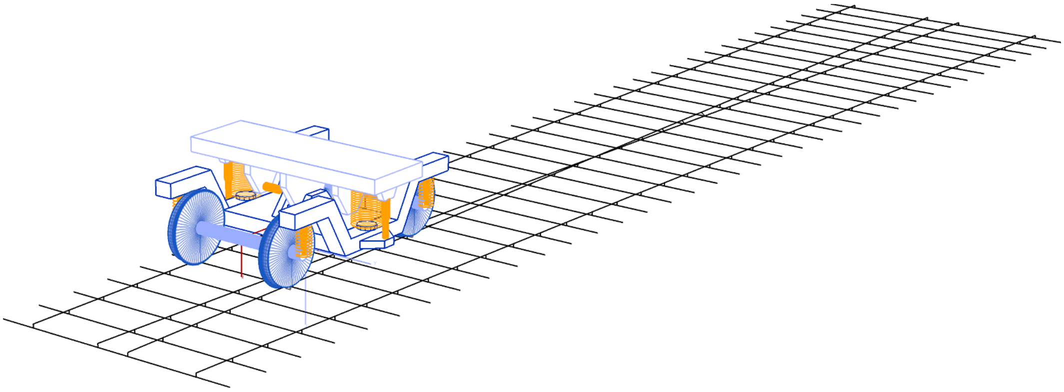

Fig. 7. MBS model of vehicle–track system (Simpack v.2019).

Table 4
Nominal MBS parameter values.

MBS model components		Value
Vehicle	Type	Single bogie [16]
	Wheel profile	S1002
	Wheel radius [m]	0.46
	Wheelset mass [kg]	1340
	Axle load [kg]	15 500
	Axle spacing [m]	2.9
Rail*	Element type	Timoshenko beam
	Node spacing along body in Simpack [m]	0.3
	Profile	UIC60/60E1
	Young's modulus [GPa]	210
	Mass density [kg/metre rail]	60
	*The crossing rail is modelled as having three times the bending stiffness and mass of the standard rail	
Rail pads	Element type	Kelvin bushing elements
	Vertical stiffness [MN/m]	120 (Nominal)60 (60E1 design)1200 (UIC60 design)
	Vertical damping [kNs/m]	25
Sleeper	Element type	Timoshenko beam
	Node spacing along body in Simpack [m]	0.25 average
	Young's modulus [GPa]	30
	Mass density [kg/m^3]	2 400
Ballast	Element type	Kelvin bushing elements
	Vertical stiffness per metre of sleeper length [MN/m/m]	30
	Vertical damping per metre of sleeper length [kNs/m/m]	125

4. Displacement reconstruction

The reconstruction of sleeper displacements can be achieved from the double integration of measured sleeper accelerations. However, this process can encounter significant corruption from low-frequency noise and short transient features of the signal. For the general case, the problem of displacement reconstruction has been widely addressed in the literature. For example, in [20] seven state-of-the-art methods for displacement reconstruction from measured accelerations are compared. Each of the seven methods is assessed with five test signals representing (1) quasi-static, (2) shaking table, (3) pedestrian bridge, (4) vehicle bridge, and (5) earthquake acceleration responses. For the five types of data, the acceleration magnitudes ranged from ± 0.01 g to ± 0.3 g. The methods are based on time-domain numerical integration and various approaches to detrend the low-frequency baselines. For six of the seven methods the computation time was less than 2 min, but for the seventh, it was between 2 and 20 h. The results showed discrepancies between the seven methods across the five tests, and there was no consistent pattern for how the different methods performed relative to one another. This can be explained by the fact that different measurement data include various types of noise and measurement errors that get amplified with the integration in different ways, suggesting that there is no proven method that can solve the displacement reconstruction problem for all possible types of acceleration data.

In the literature covering displacement reconstruction from inertial sensors, it is frequently mentioned that the main sources of disturbance that cause the above-mentioned problems come from sensor measurement error and noise at low frequencies, which result in amplified baseline distortions after integration [20–26]. The main challenges in displacement reconstruction are therefore choosing

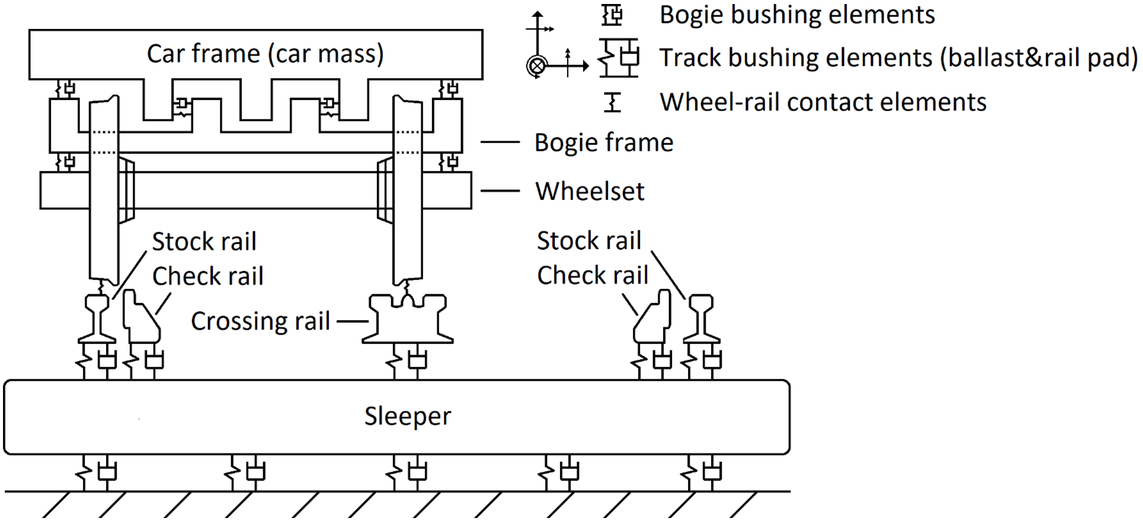

Fig. 8. 2D representation of vehicle track system during a passage through the crossing panel.

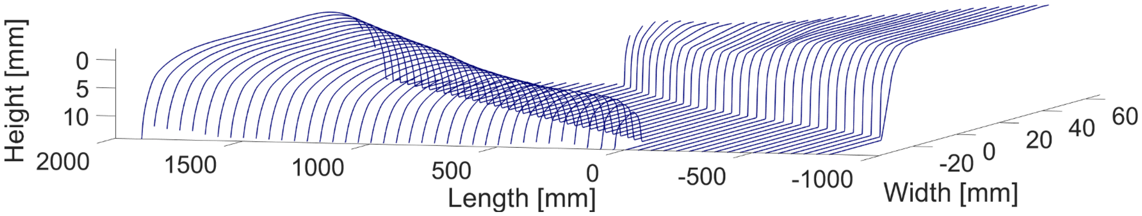

Fig. 9. Visualization of discretised rail cross-section profiles in the crossing transition. Crossing nose to the left and wing rail to the right.

the methods for high-pass filtering of the signal to remove the low-frequency noise, the integration method itself, and baseline detrending that is to be performed after an integration step to remove accumulated drift.

4.1. Primary method evaluations

Before the development of the method presented in this paper, three methods [27–29] from [20] were tested. Among the three, [27] presents a basic form for baseline adjustment by application of high-pass filters at each integration step, on which [28,29] have been developed. In addition to [27,28] introduced zero padding at both ends of the acceleration signal and least-squares linear detrending of the velocity obtained after one integration step. [29] also applies least-squares linear detrending for the acceleration signal in addition to the steps taken in [28]. In these methods, the 1/3 Simpson's integration rule was used. Variations of these methods were also evaluated as a part of this study including trapezoidal and backward rectangular integration, different high-pass filters, and additional further developments that are presented in [30] where the last reconstruction step includes polynomial fit optimisation for the baseline detrending of the integrated displacement.

The three methods [27–29] together with [30] (our prior development) were applied to recorded operational acceleration data for eight crossing panels that varied in (1) acceleration magnitudes (soft rail to sleeper connections result in magnitude ranges of ±4–20 g, and stiff rail to sleeper connections in magnitude ranges of ±20–40 g with some cases over 50 g); (2) frequency content range; (3) train axle loads; (4) train traveling directions (facing move with impact on crossing rail, or trailing move with impact on wing rail); (5) different crossing panel rail geometry condition; (6) different crossing conditions; (7) different train wheel conditions; and (8) different environmental conditions along the 110 days of monitoring. The variability in the data prevented any of the applied methods from robustly solving the displacement reconstruction problem for all cases. Particularly [30] that has added polynomial baseline detrending showed results of varying levels of bogie passage displacement signatures distortions, and high sensitivity and dependence between noise level and filter type and order (different noise levels for turnout designs with soft and stiff rail pads). Integrating observations of those methods with robustness as the key objective, the presented displacement reconstruction method was developed. Example results from methods [27–29] are given in Section 4.3.

Different Finite Impulse Response (FIR) and Infinite Impulse Response (IIR) filters were investigated for the high-pass filtering in the three tested methods. Particularly least squares and Bartlett-Hanning, Hamming, Kaiser, and Tukey window FIR filters, and Butterworth, and Chebyshev type one and two of IIR filters. It was concluded that the final displacement reconstruction results are strongly dependent on filter type and order, with additional sensitivity to chosen high-pass cut-off frequency. Generally, this indicates

Table 5
Details of MBS parameter study.

Simulation run characteristics					
Case	1	2	3	4	5
Details	Nominal crossing geometry, facing move. Ballast parameter study with vertical stiffness (a) 10, (b) 20, (c) 30, or (d) 45 MN/m/m.	Nominal crossing geometry, trailing move. Ballast parameter study with vertical stiffness (a) 10, (b) 20, (c) 30, or (d) 45 MN/m/m.	Nominal crossing geometry, facing move. Ballast parameter study with vertical stiffness 30 kN/mm, and a sleeper void of (a) 1 or (b) 2 mm for 3 consecutive sleepers, or full void (100 mm) of (c) 1 or (d) 3 sleepers.	Geometry from crossing A, facing move. Rail pad parameter study with vertical stiffness (a) 60, (b) 120, (c) 1200 MN/m.	Geometry from crossing B, facing move. Rail pad parameter study with vertical stiffness (a) 60, (b) 120, (c) 1200 MN/m.
Number of simulations	4	4	4	3	3
Total number of simulations	18				

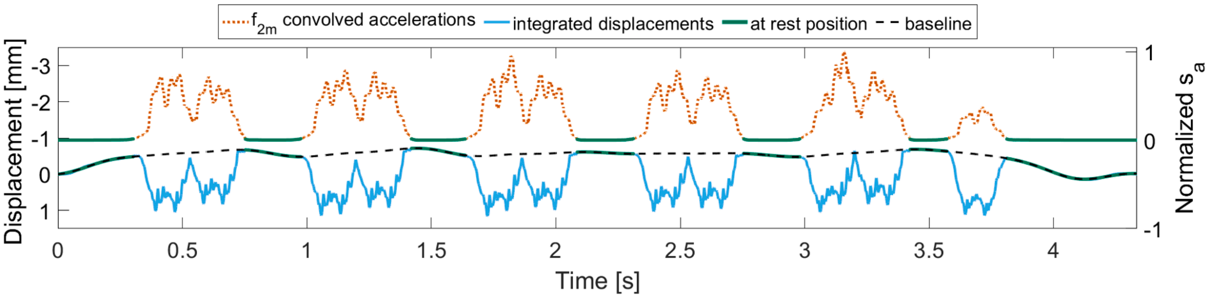

Fig. 10. Integrated sleeper displacement before baseline detrending (scale on the left ordinate), and the product of convolution between acceleration signal and moving average filter, s_a Eq. (1) (scale on right ordinate). The green segments are identified as regions between bogie passages. (For interpretation of the references to colour in this figure legend, the reader is referred to the web version of this article.)

the need for optimisation of the filter parameters for successful integration. This study concluded that time-domain filters do not provide a distinct enough cut-off between the stop and pass band for the application. It was found on the other hand that a frequency domain filter, used for example in [25], allows for filter properties that are close to the ideal "brick wall" filter with sharp transitions between stopbands and passband, which can more easily optimise and manipulate frequency content in the low-frequency region. As the signal processing of sleeper accelerations for condition monitoring is performed offline, this is a viable option. For example [21], a high-pass Butterworth filter of the fifth order is used. It has a cut-off frequency of 1.5 Hz and a sampling frequency of 1200 Hz. It can be observed in the presented plot of the filter properties that the true full cut-off frequency starts at 1.75 Hz and that the full stop band starts at 0.5 Hz. There is therefore a transition from 0.5 Hz to 1.75 Hz where the energy of the signal is gradually attenuated. If noise and information is close to one-another in the frequency spectrum around this transition, this filter will not have the precision to separate the two. In general, there are significant challenges to design a FIR or IIR filter with a low cut-off as 0.1 or 0.2 Hz (that is required in some cases), if the signal has high sampling rate and short time duration.

Lastly, in the railway field, there have been several previous papers on the reconstruction of displacements from track accelerations and velocities [21–26]. None of them addresses the reconstruction of crossing sleeper displacements from measured accelerations, however. The only paper found by the authors that is close is [31], and it focuses on the short-duration (0.4 m of train travel) rail displacement signals for individual wheel passages in a crossing transition. The displacement reconstruction problem at crossing transitions differs from the typical railway-related displacement reconstruction problems due to the need to solve both low-frequency dependent baseline distortion challenges and high-frequency and high-magnitude impact acceleration challenges. For example, in [21] it can be seen that sleeper accelerations for the plain line are in the range of ±2 g, compared to crossing sleeper accelerations that easily go above ±50 g. The variability of acceleration magnitudes for the measured accelerations can be seen in Fig. 4.

To summarise, this literature review and tests of existing methods showed that there is no exact (or unique) solution for displacement reconstruction from in-field measured accelerations and that the challenge of reconstructing displacements for railway track under both the quasi-static loading from the axle and the dynamic impact loading at the crossing transitions has few predecessors in the literature. Further, frequency domain filtering using a digital filter was identified as a way of coming closer to an ideal "brick-wall" filter for the high-pass filtering step in the displacement reconstruction algorithm. From the initial tests, it was found that the displacement reconstruction results were highly sensitive to the high-pass filter design and that a more distinct separation between stop and pass bands would be beneficial for the present application. Additionally, one of the identified problems with the methods reported in the railway literature, which is also pointed out in Barke and Chiu [32], is that too often details of the applied filtering and integration methods are missing, preventing direct implementation and testing of the used methods.

For these aforementioned reasons, the development of the displacement reconstruction method presented in this paper is based on frequency-domain filtering and digital integration. In this case, the digital integration is a natural step as data is already in the frequency domain and it only needs a division by the squared angular frequency to be transformed into displacements. Also in Brandt and Brincker [33] where a comparison is made between frequency domain integration and time domain integration, it is mentioned that trapezoidal rule integration should be avoided as it gives biased results for higher frequencies. Overall, the developed reconstruction approach showed to be suitable for 1) addressing and filtering the characteristics of the integration corruptors for the present type of acquired acceleration signals, and 2) robustly performing displacement reconstruction for large amounts of operational data that encounter different types of variability. The following subsections present the developed methodology in detail, its validation based on synthetic data and comparison to other methods, and a final discussion of the achieved displacement reconstruction. In an additional subsection, a procedure for identifying train type and speed and counting train axles from the reconstructed displacement signatures is introduced. To the knowledge of the authors, frequency domain filtering and integration have previously not been reported in the literature for the reconstruction of rail track displacement.

4.2. Methodology

In this section, a novel methodology is presented for sleeper displacement reconstruction from sleeper acceleration that has been measured during a train passage through a railway crossing panel. The methodology is based on frequency-domain integration, optimisation of the high-pass filter pass frequency, and a reconstruction relative to the “at rest position” (that is defined as the zero displacement state located before and after the train bogie passages). The full reconstruction is performed in five steps. In the following description of each step, the equations that concern the convolution and cross-correlation operations are written in continuous form, while the equations concerning the Discrete Fourier Transform (DFT) are given in the discrete form.

Step 1. The acceleration recording from one full train passage is pre-processed to identify the segments of the signal that are located between each pair of bogie passages. Initially, the acceleration recording a_d with time duration T is quadratically detrended. Further, each element of a_d is squared and spatially convolved with a 2 m moving average filter $f_{2\mathrm{m}}$ (see $f_{2\mathrm{m}}$ in Eq. (1) and Eq. (2)). In Eq. (2) M is a signal duration corresponding to a spatial length of 2 m (determined from the train speed). Finally, the segments of a_d located in-between bogie passages (here denoted s_bbp) are extracted using the criterion in Eq. (3). An example of the identified segments is shown in Fig. 10. It should be emphasised that the shape of reconstructed displacements is strongly dependent on this identified in-between bogie passages regions (“at rest position”) and this method allows for automatic identification of these segments.

$$s_\mathrm{a}(t) = \int_0^t [a_\mathrm{d}(\tau)]^2 f_{2\mathrm{m}}(t-\tau)d\tau, t \in [0, T] \tag{1}$$

$$f_{2\mathrm{m}}(t) = \begin{cases} 1/M, t \in [-M/2, M/2] \\ 0, \text{otherwise} \end{cases} \tag{2}$$

$$s_\mathrm{bbp}(t) = \begin{cases} 1, s_\mathrm{a}(t)/\max(s_\mathrm{a}(t)) < 0.02 \\ 0, otherwise \end{cases} \tag{3}$$

Step 2. After detrending, the signal is zero-padded according to Eq. (4). The zero-padding to the power of 2^n optimises the computation of the Discrete Fourier Transform (DFT) with the Fast Fourier Transform (FFT). With n equal to 19 ($N = 2^{19}$) and sampling frequency $f_\mathrm{s} = 20$ kHz, the achieved resolution in the frequency domain is about 0.04 Hz. This step allows for smoother high-pass filtering at low frequencies compared to what would have been achieved by a DFT with a frequency resolution of about 0.2 Hz corresponding to a typical train passage duration of 5 s.

$$a_\mathrm{dz}(t) = \begin{cases} a_\mathrm{d}(t), t \in [0, T] \\ 0, t \in (T, N/f_\mathrm{samp}] \end{cases} \tag{4}$$

Step 3. The Frequency Domain Integration (FDI) is performed. The zero-padded signal $a_\mathrm{dz}(t)$ is discretised to $a_\mathrm{dz}[n]$ with n limits $[-N/2, N/2-1]$ formed for obtaining a symmetric DFT. Next, $a_\mathrm{dz}[n]$ is transferred to the frequency domain via a DFT, see Eq. (5). In Eq. (6) an angular frequency domain is defined and used in Eq. (7) to obtain a transfer function $H[k]$ for the double integration in the frequency domain. Further, the frequency-domain acceleration signal $A_\mathrm{dz}[k]$ is element-wise multiplied with the digital integrator $H[k]$ and subjected to the frequency-domain high-pass filter at a frequency f_p where the parameter p is the corresponding sample number, see Eq. (8). The high-pass filter frequency is optimised in Step 5. Next, this signal is transformed back to the time domain with the IDFT, see Eq. (9). The result of Step 3 is displacements $d_\mathrm{int}[p, n]$ that are dependent on the parameter p. The obtained displacements $d_\mathrm{int}[p, n]$ are of length T with zero phase shift relative to the initial acceleration signal.

$$A_{dz}[k] = \sum_{n=-N/2}^{N/2-1} a_\mathrm{dz}[n]e^{-\frac{i2\pi k}{N}n}, \ -N/2 \le k \le N/2-1 \tag{5}$$

$$\omega[k] = \frac{2\pi f_\mathrm{s}}{N}k, N/2 \le k \le N/2-1 \tag{6}$$

$$H[k] = \begin{cases} -1/(\omega[k])^2, N/2 \le k \le N/2-1 \\ 0, k = 0, \end{cases} \tag{7}$$

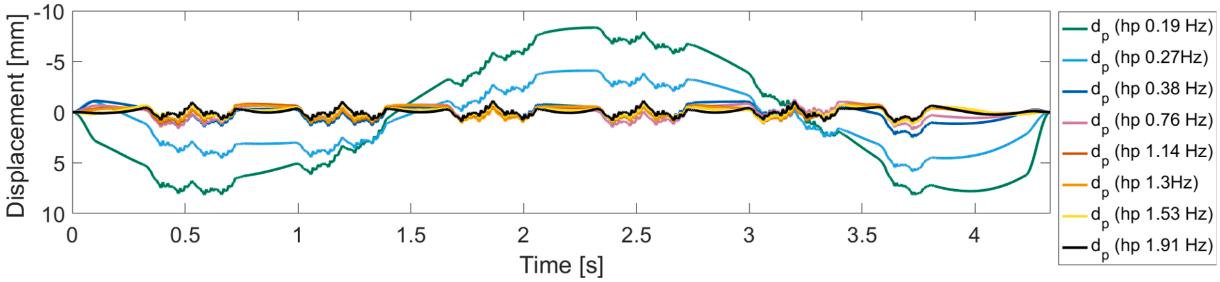

Fig. 11. Integrated sleeper displacement for different high-pass frequencies f_p before in-between-bogie baseline detrending.

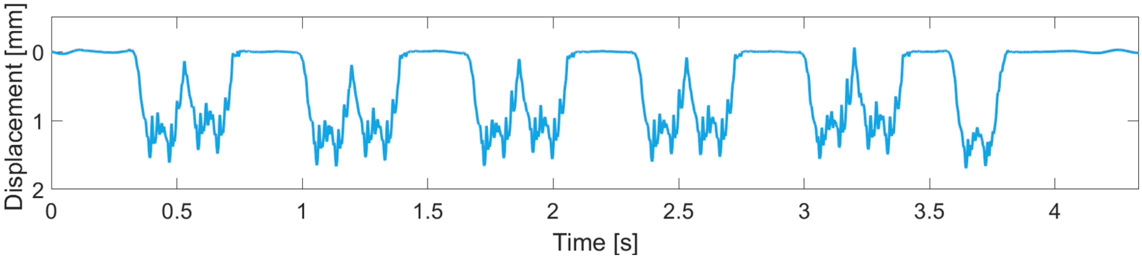

Fig. 12. Example of final reconstructed displacement from the displacement reconstruction algorithm with the optimum $f_p = 1.3$ Hz. Signal from X2 train with the first bogie passages discarded due to a signal corrupting sensor wake-up transient.

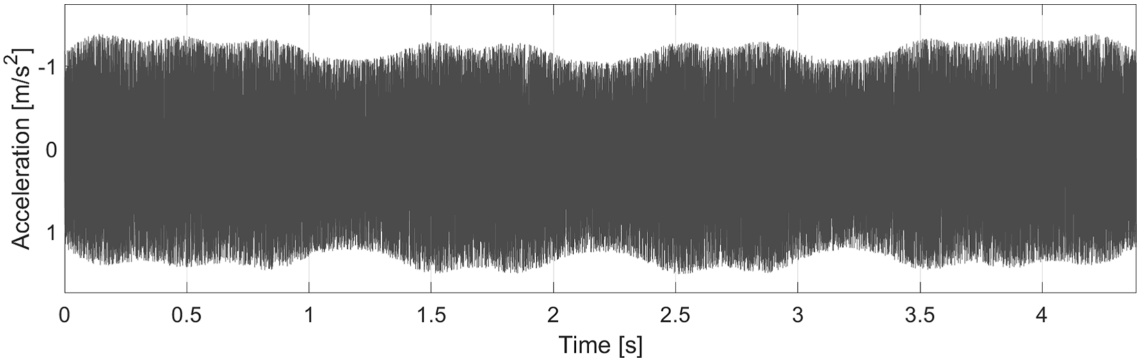

Fig. 13. Noise signal that is superposed to the simulated accelerations. The pulsating effect represents the possible variation in noise levels during axle passages.

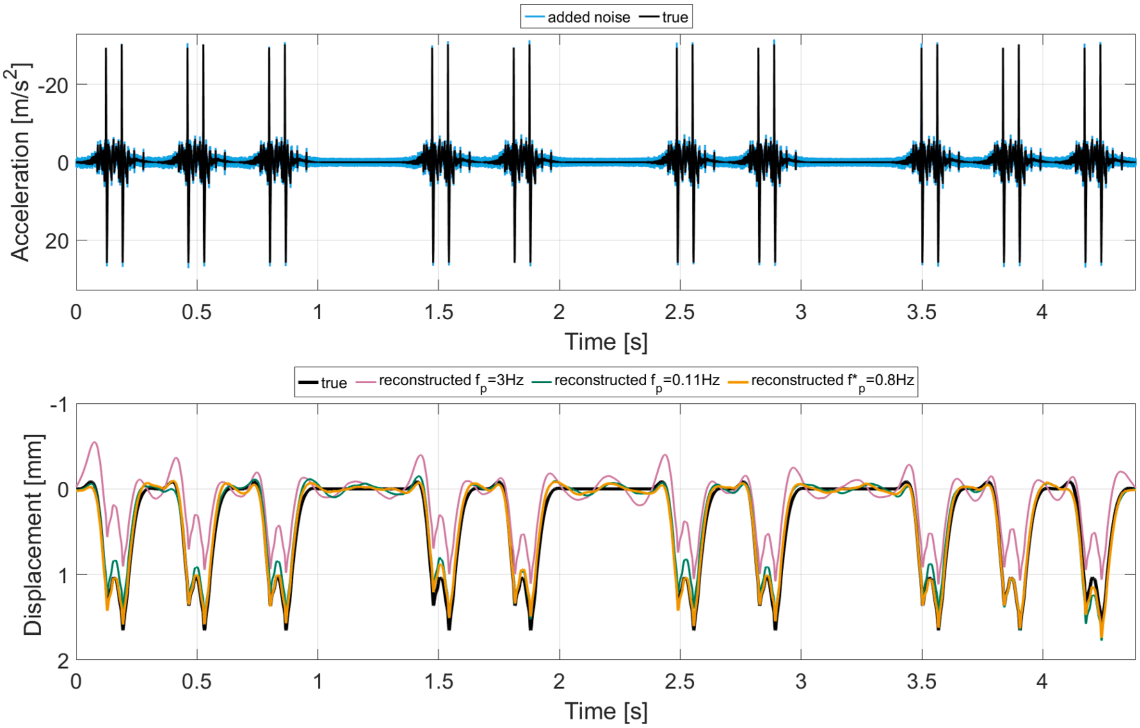

Fig. 14. Acceleration (top) and displacement (bottom) results for validation of the displacement reconstruction method. The mean of the maximum displacements per axle passage is 1.51 mm for the true results and 1.48 mm for the reconstructed displacement with $f_p^* = 0.8$**Hz**.

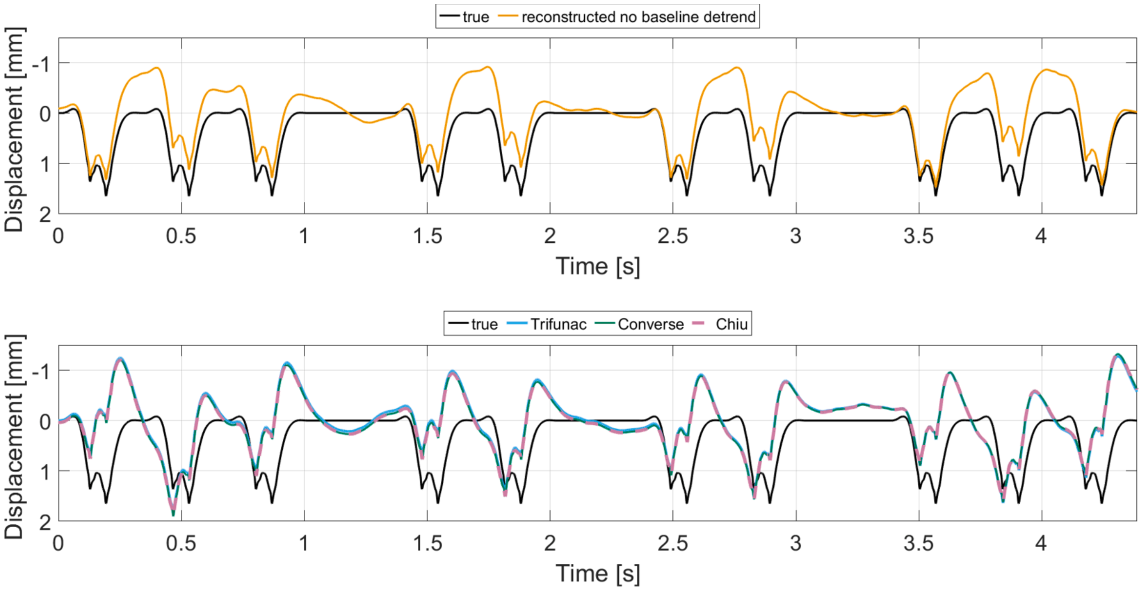

Fig. 15. Results for (1) this paper's displacement reconstruction method without the in-between bogie region baseline detrending part and 0.8 Hz digital high-pass filter (top), and (2) three displacement integration methods, Trifunac [27], Converse [28] and Chiu [29] with 0.8 Hz high-pass 6th order IIR filter (bottom). True simulated displacements are added to both figures for reference. All integration results stem from simulated acceleration data with the same added noise.

$$D[p,k] = \begin{cases} A_{dz}[k]H[k], -N/2 \leq k < -p, \\ 0, -p \leq k \leq p, \\ A_{dz}[k]H[k], p < k \leq N/2 - 1, \end{cases} \quad 0 < p \leq N\frac{f_0}{f_s}, f_p = \frac{f_s}{N}p \tag{8}$$

$$d_{\text{int}}[p,n] = \frac{1}{N}\sum_{k=-N/2}^{N/2-1} D[p,k]e^{\frac{i2\pi k}{N}n}, \ -f_s T/2 \leq n \leq f_s T/2 - 1, 0 < p \leq N\frac{f_0}{f_s} \tag{9}$$

Step 4. The integrated displacements d_{int} are detrended to the "at rest position". This is achieved by a linear fit b_f to the displacement curve d_{int} at the identified locations s_{bbp} between bogie passage locations from Eq. (3). The obtained curve b_f is smoothened with a 10-metre wavelength low-pass filter. The obtained filtered curve b_{f10m} is used as a baseline detrend. It is subtracted from d_{int} to obtain the baseline detrended displacements d_{bd}, see Eq. (10) and Fig. 10.

$$d_{\text{bd}}[p,n] = d_{\text{int}}[p,n] - b_{\text{f10m}}[p,n], n = [-f_s T/2, f_s T/2 - 1], 0 < p \leq N\frac{f_0}{f_s} \tag{10}$$

Step 5. The final step of the displacement reconstruction is to find the optimum value p for the high-pass filter frequency f_p. As the value of p increases, shorter time windows of displacements d_{bd} obtain zero mean due to the high-pass filtering. This means that above a certain p, the displacement signatures of individual bogie passages will become distorted. This will be observed as curve oscillations around the detrended baseline at the beginning and end of each bogie passage, which means that the magnitude of negative (upwards) displacements will start to increase. In the optimisation of p, a penalty is set for these negative displacements. The objective function in the optimisation also accounts for the standard deviation of d_{bd}. The standard deviation will start to increase if the d_{bd} baseline detrend

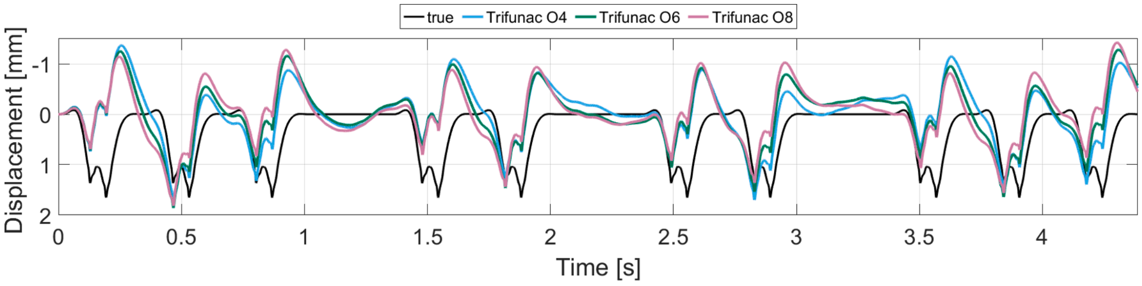

Fig. 16. Displacement integration method of Trifunac [27] with 4th, 6th, and 8th order IIR Butterworth filter with 0.8 Hz high-pass frequency. True simulated displacements are added for reference. All integration results concern simulation acceleration data with the same added noise.

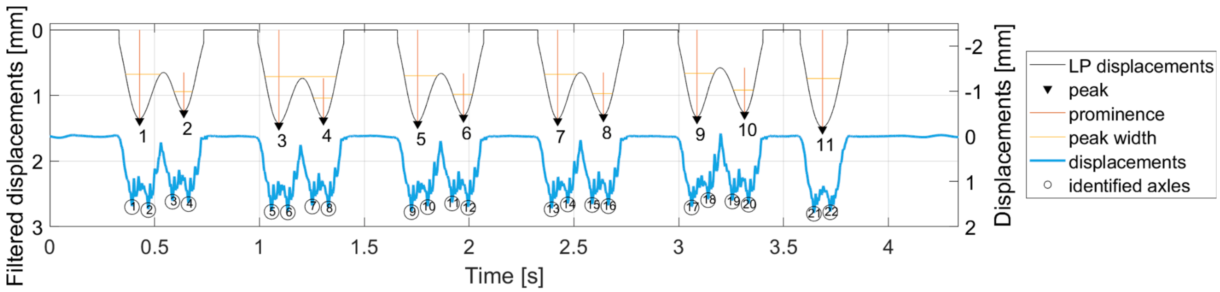

Fig. 17. Identification and count of train axles.

residuals get higher due to low-frequency noise, or if d_{bd} encounters local distortions or global inclinations. Finally, the objective function is computed as a multiplication of these two functions and the product is minimized in the optimisation, see Eq. (11).

The optimisation is performed in two steps for frequencies between 0 and $f_0 = 2$ Hz. The first step is an exploration of the domain with a step length of 0.2 Hz for f_p. The second step is a fine optimisation with a 0.04 Hz discretization step in the localized domain obtained from the initial exploration. Reconstructions in the optimisation domain obtained with this exploration are presented in Fig. 11. It shows various curves d_{int} with different baselines. Each of the bogie passage segments will be affected differently by the baseline detrend after subtracting $b_{\mathrm{f10m}}[p,m]$.

With the presented optimisation scheme, a stable displacement reconstruction is secured. The complete displacement reconstruction method is developed to allow for large sets of data and long-term automatic processing of accelerations from the field with variable operational conditions and varying quality of measured data. An example of the result of the reconstructed displacement is presented in Fig. 12.

$$p = \operatorname{argmin}\left(\left(\sum_{n=0}^{M-1}(d_{\mathrm{bd}}[p,n] < 0)\right)\sigma_{\mathrm{bd}}\right), 0 < p \leq N\frac{f_0}{f_{\mathrm{samp}}} \tag{11}$$

4.3. Displacement reconstruction validation

Validation of the presented displacement reconstruction methodology has been performed using synthetic acceleration and displacement data. Acceleration data has been assembled from simulation results of individual bogie passages from the MBS model and has been corrupted with noise. It concerns the simulated case with 10 MN/m/m ballast stiffness (Case 1 in Table 5). Small and large wagon bogie spacings are used to test the algorithm, but the bogie spacing pattern does not have a physical counterpart. The reconstructed displacements are first compared to true displacements and thereafter the developed method is contrasted to results from the three methods [27–29] referenced in Section 4.1.

The applied noise is set to have an RMS equal to 20% of the RMS of the original acceleration signal. It is constructed as a combination of (1) a random white noise signal (spectrum 0–5000 Hz), (2) a low-frequency sine wave ($f = 1/2T$ where T is the time duration of the signal) with a magnitude equal to 5% of the initial magnitude of the random white noise, and (3) a pulsating scaling function that increases noise levels up to 1.2 for axle passage regions (it scales the superimposed noise parts (1) and (2)). The complete noise signal is presented in Fig. 13. The low-frequency sine wave can be observed from the mild global curvature.

Fig. 14 shows true simulated accelerations with and without noise (top) and true simulated displacements and displacements reconstructed from simulated accelerations with added noise using the presented method (bottom). The optimal high-pass frequency in this case is $f_p^* = 0.8$Hz. Results are shown also for $f_{\mathrm{p}} = 0.11$Hz and $f_{\mathrm{p}} = 3$Hz. The low f_{p} case shows a higher level of variation of the maximal displacements per axle passage than the optimal frequency, and the high f_{p} case shows that displacement energy is cut if the low pass frequency is too high. The mean error for the maximum displacement per axle passage in this test is 1.96% (1.509 mm true and 1.48 mm reconstructed). Without added noise, the reconstructed displacements are in more or less perfect agreement with the true signal (not shown). In conclusion, this validation example demonstrates a good accuracy of the proposed displacement reconstruction methodology both in terms of the mean of the maximum sleeper displacements and the shape of the sleeper displacement signature due to a bogie passage.

Fig. 15 compares results for the three displacement reconstruction methods Trifunac [27], Converse [28] and Chiu [29] discussed in Section 4.1 to the method presented in this paper without the in-between bogie region baseline detrending. The baseline detrending is removed to obtain a direct comparison between the displacement reconstruction techniques. The true signal is included for reference. The applied high-pass filter for the literature methods is a 6th-order IIR Butterworth filter, and the integration of accelerations is performed using the 1/3 Simpsons integration rule. All methods perform reconstruction from simulated accelerations with added noise and use a 0.8 Hz high-pass frequency. It can be observed that even though all of the methods need baseline detrending, the frequency domain filtering and integration provide more regular signal and bogie passages. It thus provides a better basis for robust displacement reconstruction results for the present type of acceleration signals as outlined in Section 4.1. It should also be noted that reconstruction without noise leads to less distorted bogie passage signatures but the relative comparison between the methods is similar as with noise (not shown). Finally, Fig. 16 presents variations of the Trifunac results from Fig. 15. Here the 6th-order IIR Butterworth filter result is complemented with results generated using 4th and 8th order filters of the same type. It can be observed that the results are highly sensitive to the choice of filter order which requires careful tuning of the filter for given conditions and thus reduces the robustness of this type of filter as outlined in Section 4.1.

4.4. *Identification and location of train axles*

After the displacement reconstruction, the passing of each train axle is identified in the signal and counted. This is performed by first identifying the centre of each bogie using the “findpeaks” MATLAB function. This is performed for displacement data that has been low-pass filtered at a wavelength of 10 m. Low-pass filtering is required as the sleeper displacement signatures for individual bogie passages may have multiple sharp peaks. Thus, multiple peaks can be identified in the region of an individual axle passage, see the displacement signatures in Fig. 17. MATLAB “findpeaks” function is run with prescribed peak prominence (depth) and peak width. To have a robust identification of axle passages, the low-pass filter concentrates energy around the centre of the bogie within a ±2 m region. Each bogie is then identified as a local maximum in the low-pass filtered sleeper displacement. Two additional axles, for each bogie, are identified from the maximal reconstructed displacement values. The identified axles are presented as the 22 circled peaks in Fig. 17. The information on located axles is later used in the post-processing of long-term data.

4.5. *Discussion*

Sleeper displacement is a relative quantity that can be used for a quantitative interpretation of S&C condition monitoring data, for example, to better understand the current sleeper support conditions. But displacements are difficult to measure. In contrast, sleeper acceleration is an absolute quantity that is more practical to measure. But, solely observed sleeper accelerations mainly have a qualitative interpretation, whereas addressing them quantitatively requires a calibrated MBS analysis. This section has presented a methodology to determine sleeper displacement as an indirectly measured quantity reconstructed from sleeper acceleration.

This reconstruction process is significantly affected by the transient nature of the signal, with the inherent difficulty to filter out the low-frequency transient features. For comparison, consider the definite integral of a single-frequency harmonic function where the upper bound is a variable. The resulting harmonic signal obtains a constant offset apart from the integration constant. This offset is dependent on the initial harmonic phase where the integration was started. Further, by considering the integration of a wide-spectrum noisy transient signal, also the corresponding integration offset becomes transient and noisy. A double integration amplifies any noise in this offset. Concerning the field measurement data that includes measurement noise of a random nature, the integration noise amplification encounters some weight of random nature. These overviewed challenges significantly affect the integration of displacements from measured accelerations. To sum up, the integration corruptors are identified to be short transients of low-frequency noise, together with general measurement noise that is amplified in the process of numerical integration.

In this paper, a stable solution is found by carrying out the displacement reconstruction relative to the “at rest position” from the regions between bogie passages. In addition, the integration is performed in the frequency domain for a more flexible reconstruction that can finely address the features of the signal at low frequencies in the range of 0 – 2 Hz. In terms of filtering in the time domain, it has been observed that the nonlinear phase of IIR filters strongly affects the integration of this type of transient signals. Additionally, FIR filters with linear phase encounter difficulties in the fine-tuning of the high-pass stop band in the frequency region 0 – 2 Hz at a 20 kHz sampling rate.

The method has been verified using MBS synthetic data showing true simulated and reconstructed displacements. Based on the literature survey and the analysis presented in this paper, it is concluded that there is no exact solution to this problem and that the quality of the reconstructed displacements is significantly influenced by the quality of the acceleration measurements.

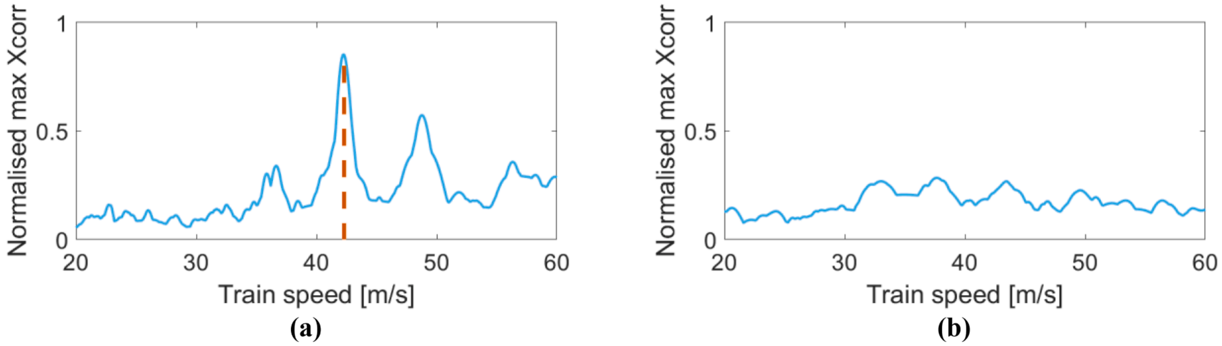

Fig. 18. Examples where the train passage is (a) identified or (b) not identified as an X2 high-speed passenger train. Continuous line presents max $c_v(t)$, while the dashed line presents the identified train speed, see Eq. (14).

5. Train type and speed identification

The operational environment for the eight crossing panels listed in Table 1 contains large variability. The variability comes from different train types (passenger and freight trains), axle loads, train speeds, wheel profiles, climate conditions, etc. To obtain more accurate information about the traffic loading associated with the condition monitoring data, a train speed and train type identification method has been developed. The method operates by cross-correlating new acceleration signals from passages by unknown trains with reference signals from known train passages. For the known train passages, the train type and speed have been manually identified by matching the axle locations of a given train type to the acceleration peaks in the signal. All signals are low-pass filtered at 20 Hz before the cross-correlation is computed. For this frequency range, it is observed that the sleeper displacement signature due to each axle passage will be smooth and dominant and that similarities between different signals indicate the same train axle composition. The initial sampling frequency of 20 kHz is resampled to 1 kHz because the process is computationally intensive. Reducing the signal vector length by 20 times significantly reduces the computational effort while the accuracy is not affected as the signals are low-pass filtered to 20 Hz. In the reference signals the first and last bogie passages are removed to make the signal symmetrical (same for facing and trailing move), and to avoid interference from the sensor wake-up transients that are present in the measured signals. Due to this procedure, the remaining axles for X2 and X31 passenger trains have similar axle dispositions, thus these two train types are identified together.

In the algorithm, each reference signal is first resampled to the train speed range from 20 to 60 m/s at intervals of 0.1 m/s. A small speed increment is used as the method is sensitive to train speed. The reference signals are named $a_{v-\mathrm{ref}}$ with length $T_{v-\mathrm{ref}}$, where v indicates the associated train speed. Each reference signal is normalised by its RMS value, and the new signal to be evaluated a_{lp20Hz} (with length T), is also RMS-normalised. Then the signals are cross-correlated according to Eq. (13) for all sampled train speeds from 20 to 60 m/s.

When an RMS-normalised signal is cross-correlated with itself, the maximum product is equal to 1. In this paper, if the satisfaction criterion in Eq. (14) (80% similarity) is fulfilled, the new acceleration recording is classified as the identified train type with the corresponding train speed from Eq. (14). An example of the function $\max(c_v(t))$, where an X2 high-speed passenger train is identified, is shown in Fig. 18(a). Another example, where the train passage is not identified as an X2 or X31 train, is presented in Fig. 18(b). For each monitored crossing panel, a different set of reference acceleration signals needs to be created for the X2 and X31 trains. To increase the accuracy of the method, multiple reference signals are stacked together (time-wise continuation), see Eq. (12).

$$a_{v-\mathrm{ref}}(t) = [a_{v-\mathrm{ref}\ 1}(t), a_{v-\mathrm{ref}\ 2}(t), \cdots, a_{v-\mathrm{ref}\ \mathrm{n}}(t)], v \in [20, 20.1, 20.2, \cdots, 60]\mathrm{m/s} \tag{12}$$

$$c_v(t) = \int_{-T}^{T_{\mathrm{v-ref}}+T} a_{v-\mathrm{ref}}(\tau) a_{\mathrm{lp20Hz}}(t+\tau) d\tau, t = \left[0, T_{\mathrm{ref}} + T\right], v \in [20, 20.1, 20.2, \cdots, 60]\ \mathrm{m/s} \tag{13}$$

$$v_t = v \mathrm{for} \max(c_v(t)) \mathrm{if} \max(c_v(t)) > 0.80, v \in [20, 20.1, 20.2, \cdots, 60]\mathrm{m/s} \tag{14}$$

Additional analyses were performed to evaluate the possibility of identifying X2 and X31 trains separately. It was concluded that by increasing the Eq. (14) threshold to 0.95 it is possible to achieve this separation for the crossing panels in Höör. This is due to the resilient rail pads in the Höör crossing panels that attenuate the response at higher frequencies, leading to less variability in acceleration responses at the sleeper. For the Stehag crossing panels with direct rail to sleeper fixing design, no clear separation between X2 and X31 trains was achieved when all train passages were considered. A separation could be achieved by manually selecting signals that were not affected by wake-up noise and where the full train composition was accounted for. No further efforts were made to improve the accuracy of the train identification method as its main purpose in the present investigations is to reduce operational variability by extracting measurement signals from known train types. Also, the latest generation of the utilised sensors record data without wake-up noise, so better precision is expected in future studies solely from the availability of higher quality data that allows for full reference signals to be used for each train type.

There are other forms of train identification algorithms reported in the literature. In [34], multiple accelerometers are installed in plain line track and a feature extraction method is used to identify trains with 97% accuracy. In [35], several neural network-based train-type identification methods are tested using data from S&C instrumented with multiple accelerometers. Among the tested methods, it is concluded that a convolutional neural network gives the best performance. The identification is based on the locomotive segment of the signal and for the seven investigated locomotive classes accuracies were 37.5%, 44.0%, 47.7%, 81.5%, 87.9%, 88.7%, and 92.2%. Overall, machine learning algorithms resolving annotation and identification problems are known to be successful in many practical applications. Compared to [34,35], the presented method shows robustness with practically no training needed, and it uses only one accelerometer. In conclusion, comparing the presented method to other train-type identification methods based on machine learning or feature extraction "black-box" procedures, this method operates within the "white-box" domain and is based on knowledge of the physical system.

6. Analysis of bogie passage sleeper displacement signatures

In this section, results from the experimental and numerical (MBS) analyses are presented and compared. In Section 6.1, reconstructed sleeper displacements are shown for individual bogie passages in the eight instrumented crossings. Results from simulations with their comparison to the measurement results are presented in section 6.2.

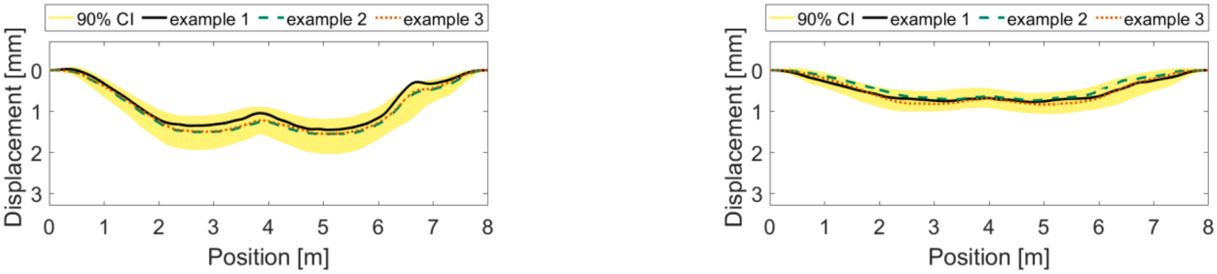

(a) (b)

Fig. 19. Reconstructed sleeper displacements for X2 and X31 train bogie passages with axle loads of 15.5 and 13 tonnes: (a) Höör 21a – trailing move, and (b) Höör 21b – trailing move.

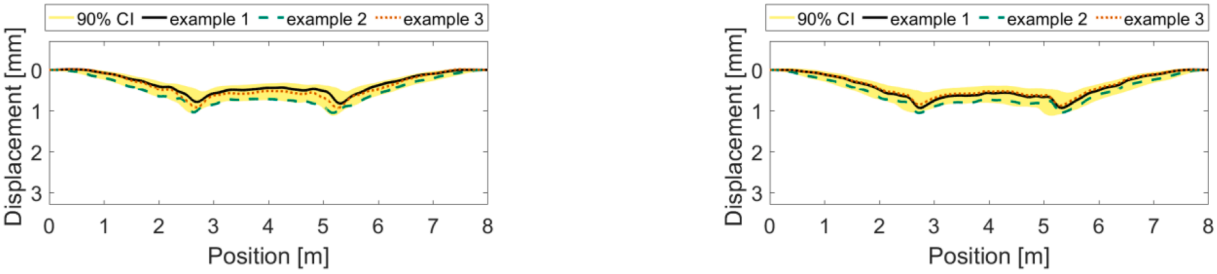

(a) (b)

Fig. 20. Reconstructed sleeper displacements for X2 and X31 train bogie passages with axle loads of 15.5 and 13 tonnes: (a) Höör 22a – facing move, and (b) Höör 22b – facing move.

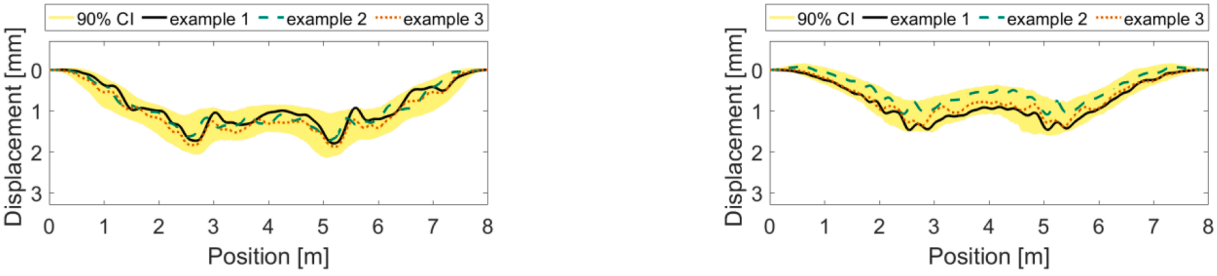

(a) (b)

Fig. 21. Reconstructed sleeper displacements for X2 and X31 train bogie passages with axle loads of 15.5 and 13 tonnes: (a) Stehag 21a – facing move, and (b) Stehag 21b – facing move.

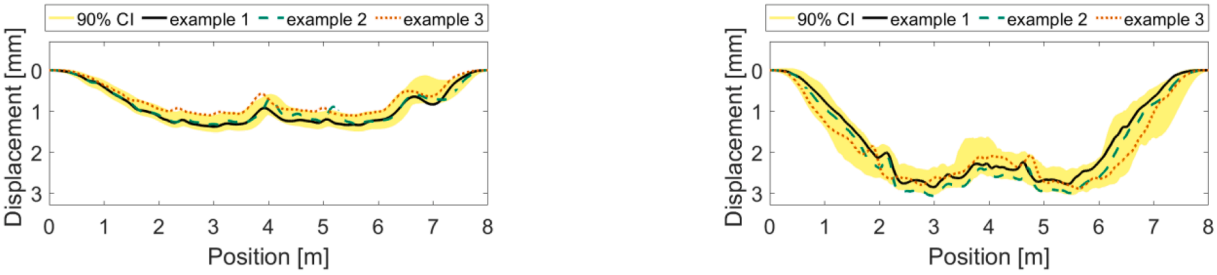

(a) (b)

Fig. 22. Reconstructed sleeper displacements for X2 and X31 train bogie passages with axle loads of 15.5 and 13 tonnes: (a) Stehag 31a – trailing move, and (b) Stehag 32b – facing move.

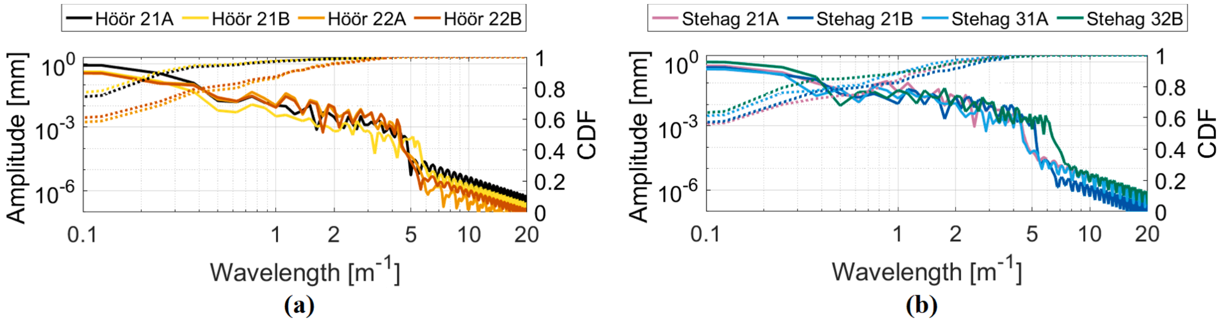

Fig. 23. Single sided spatial FFT of individual bogie passage sleeper displacement signatures for (a) Höör and (b) Stehag crossing panels. Processed signals correspond to the 'example 1′ displacements presented in Figs. 19 to 22.

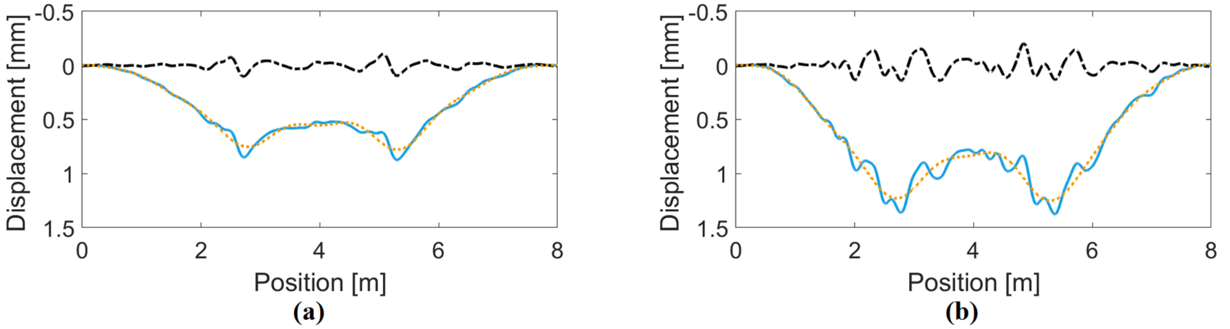

Fig. 24. Sleeper displacement signatures for a single bogie passage at (a) Höör 22b and (b) Stehag 21b. Raw data (solid line), band-pass filtered data of 1.0 – 0.1 m wavelengths (dashed line, Höör 22b: RMS = 0.031 mm, Stehag 21b: RMS = 0.065 mm), and filtered above 1 m wavelengths (dotted line).

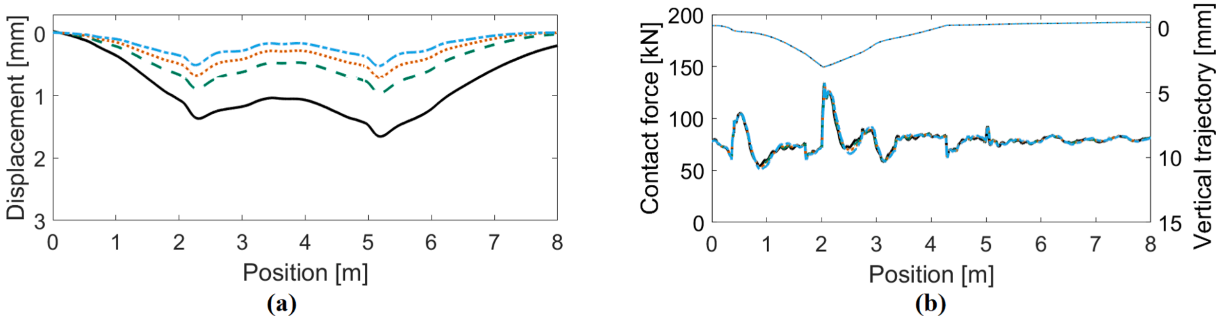

Fig. 25. Simulated influence of linear ballast stiffness on (a) vertical sleeper displacement, and (b) vertical wheel–rail contact force and relative wheel–rail kinematic trajectory (thinner lines). Results for the baseline simulation case 1, given in Table 5, are plotted as (a) continuous, (b) dashed, (c) dotted, (d) dot-dash lines.

6.1. *Reconstructed displacement signatures for eight instrumented crossings*

For the crossing panels at Höör (Fig. 19 and Fig. 20) and Stehag (Fig. 21 and Fig. 22), this subsection presents signatures of reconstructed sleeper displacements from identified X2 and X31 passenger trains. The presented displacement signatures concern bogie passages for the last bogies in the train composition. This is to exclude the interference of two adjacent wagons bogie passages on the displacement signatures. The corresponding axle loads are 15.5 tonnes for the X2 train, 13 tonnes for X31. The observed train speed range is approximately 80 to 180 km/h, with two more prominent speeds of 110 and 160 km/h. The two different axle loads and variability in train speed, passenger load, and environmental conditions together contribute to the variability in the presented results. Additionally, as described previously, the turnouts in Höör are of a newer design with soft rail pads, while the turnouts in Stehag are of an older design with a stiff direct fixing of the crossing rail to the sleepers. Each figure shows three selected examples of reconstructed displacements and the 90% confidence interval for the 110 days of monitoring.

A significant variation in sleeper displacement signatures is observed between the eight crossing panels in terms of smoothness and

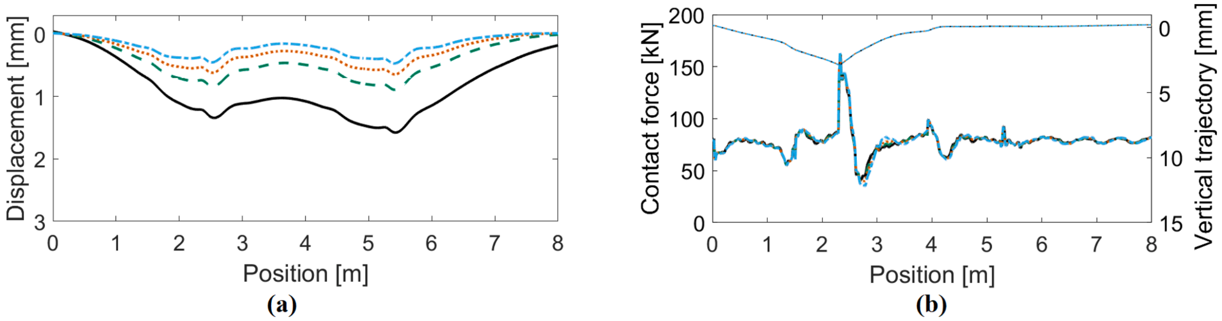

Fig. 26. Simulated influence of linear ballast stiffness on (a) vertical sleeper displacement, and (b) vertical wheel–rail contact force and relative wheel–rail kinematic trajectory (thinner lines). Results for the baseline simulation case 2, given in Table 5, are plotted as (a) continuous, (b) dashed, (c) dotted, (d) dot-dash lines (stiffness increasing order).

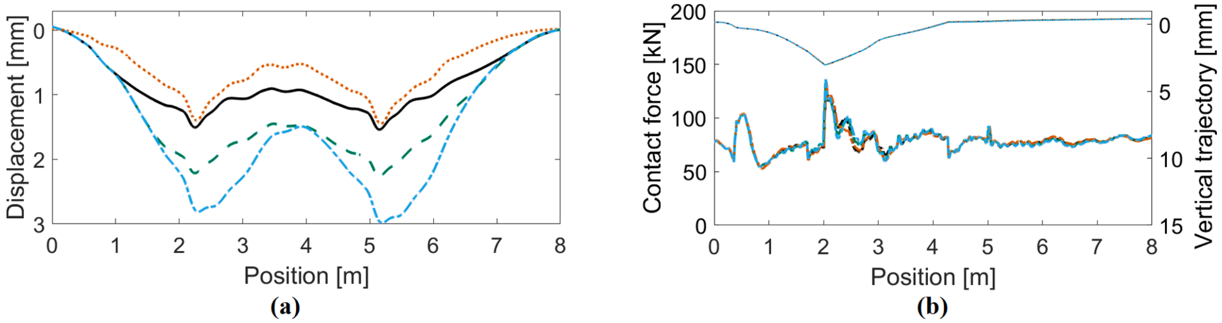

Fig. 27. Simulated influence of voided sleeper conditions on (a) vertical sleeper displacement, and (b) vertical wheel–rail contact force and relative wheel–rail kinematic trajectory (thinner lines). Results for the baseline simulation case 3, given in Table 5, are plotted as (a) continuous, (b) dashed, (c) dotted, (d) dot-dash lines (order, 1 and 2 mm void at 3 sleepers, and full void at 1 and 2 sleepers).

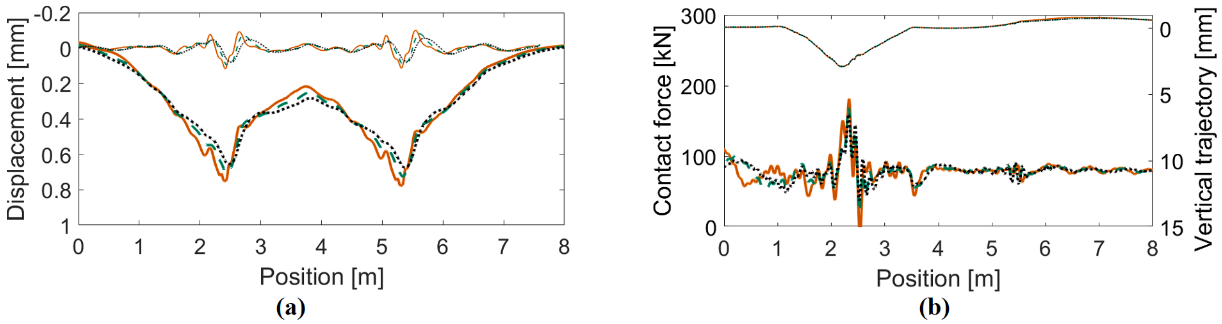

Fig. 28. Simulated influence of rail pad stiffness on (a) vertical sleeper displacement (thin lines 1.0–0.1 m band-pass filtered displacements), and (b) vertical wheel–rail contact force and relative wheel–rail kinematic trajectory (thinner lines). Load case 4, see Table 5. The RMS for the band-pass filtered displacements are 0.025 mm (K_{pad} = 60 MN/m – dotted lines), 0.028 mm (K_{pad} = 120 MN/m – dashed lines) and 0.029 mm (K_{pad} = 1200 MN/m – continuous lines).

magnitude. There is a group difference between the turnouts in Höör (new design) and Stehag (old design) in the sense that the displacement signatures from Stehag are on average less smooth. It can also be noted that smoother displacement signatures are found for the trailing move crossings, see Fig. 19(a) and Fig. 22(a). The range of the 90% confidence interval varies significantly between the different crossing panels. This effect is linked to the variability in maximum sleeper displacement over time.

Even though there is some variability in the results, it can be concluded that the displacement signatures are distinct for each crossing panel. Thus, the displacement reconstruction methodology provides a robust and stable, but not unique, reconstruction using the data for a narrowed train-type analysis. Depending on the noise levels in the acceleration measurements, different levels of corruption are expected to be present in the reconstructed sleeper displacement.

From a condition monitoring perspective, the question is what information could be extracted from the sleeper displacement signatures. The global displacement signature is governed by the quasi-static track deformation under the bogie axles and contributes

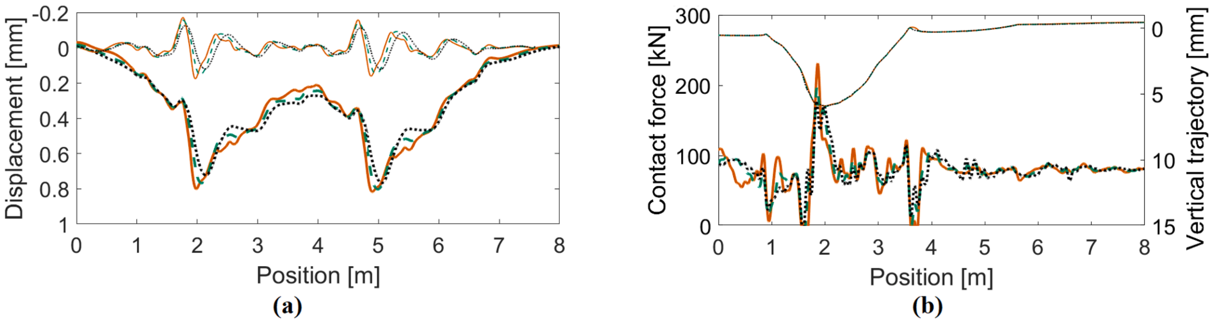

Fig. 29. Simulated influence of rail pad stiffness on (a) vertical sleeper displacement (thin lines 1.0 – 0.1 m band-pass filtered displacements), and (b) vertical wheel–rail contact force and relative wheel–rail kinematic trajectory (thinner lines). Load case 5, see Table 5. The RMS for the band-pass filtered displacements are 0.045 mm ($K_{pad} = 60$ MN/m – dotted lines), 0.051 mm ($K_{pad} = 120$ MN/m – dashed lines) and 0.048 mm ($K_{pad} = 1200$ MN/m – continuous lines).

to most of the sleeper displacement. As the magnitude of the sleeper displacement is proportional to the support stiffness provided by the ballast [8], the ballast condition can be observed via the quasi-static deformation. In Milne et al. [19], a beam on elastic foundation model was used to show that the quasi-static track deformation is more or less fully described by longitudinal track deformation wavelengths above one metre. In Fig. 23, the spatial FFT of the sleeper displacement signature is shown for individual bogie passages from the eight Höör and Stehag crossing panels. For the present cases, it was observed that the signal contents down to 0.5 m wavelength (2 m^{-1}) account for 90–99% of the total displacement energy depending on the crossing panel. Further, field measurements showing the influence of sleeper voids on signatures of rail accelerations and displacements are reported in [6,23] and a correlation can be observed between them and the signatures of the above-shown crossing panels with larger displacement magnitudes. The similarities concern indication of multiple impacts and generally higher frequency content of the signal for voided sleepers. But it should be noted that refs. [6] and [23] address displacements for voided sleepers for regular tracks and not the crossing panels where impacts occur due to wheel transition from the wing rail to the crossing nose (and vice versa). It can also be seen in Milosevic et al. [36] that multiple impacts can occur in crossing transition due to poor crossing rail and wing rail geometry quality, thus signatures of multiple impacts might not be a direct indicator of voided sleeper.

As there are irregularities in the displacement signatures, this is an indication of additional dynamic excitation stemming from for example the excitation by the wheel and crossing rail geometry above the quasi-static wavelength range. To further analyse these irregularities, the quasi-static track deformation has been filtered out from the sleeper displacement signatures via a band-pass filter in the spatial domain for 1.0 – 0.1 m wavelengths (corresponding to 40 – 400 Hz at train speed 40 m/s). The lower one-metre limit is taken from Milne et al. [19], while the shorter wavelength limit of 0.1 m is to bound the signal from possible high-frequency noise. For a single bogie passage in the crossing panels at Höör 22b and Stehag 21b, example results for this signal processing are shown in Fig. 24. As indicated by the RMS values for these band-passed signals, there can be significant differences in the signal energy between different crossing panels in this frequency range. The interpretation of this signal will be further discussed in Section 6.2.

6.2. Simulation results for displacement signature interpretation

Results from simulations with the MBS model, using the input data and cases listed in Table 5, are presented in Figs. 25 to 29. The subfigures on the left show the calculated sleeper displacement signature at the location corresponding to the sensor position (the first sleeper after the crossing nose) and are thus analogous to the reconstructed displacements in Figs. 19 to 22. The subfigures on the right illustrate the vertical wheel–rail contact force and the wheel–rail relative vertical displacement for the front wheel of the bogie on the crossing rail side (leading wheel). The latter thus represents the dip-shaped kinematic motion between the wheel and crossing rail which is the displacement excitation that causes the force peak observed in the figures. The horizontal axis in the figures to the left relates to the position of the centre of the bogie, while for the figures to the right it relates to the position of the leading wheel. In both cases, the simulated distance is 8 m.

The influence of linear ballast properties in facing (Fig. 25) and trailing moves (Fig. 26), nonlinear ballast properties (Fig. 27), crossing rail geometry, and rail pad properties (Fig. 28 and Fig. 29) on the calculated sleeper displacement have been studied. In Fig. 25 and Fig. 26, it is observed that a reduction of ballast stiffness from the reference value 30 MN/m/m to 10 MN/m/m increases the maximum sleeper displacement from 0.71 mm to 1.65 mm for the facing move, and from 0.65 mm to 1.58 mm for the trailing move. For each given traffic direction, the time-variant wheel–rail contact force is similar in magnitude for all studied ballast conditions. For the trailing move, slightly smoother sleeper displacement signatures are observed with lower maximum values, but the wheel–rail contact forces are higher for this nominal crossing geometry. It can be noted that the model produces similar wheel-rail contact forces at the crossing transition as those measured with an instrumented wheelset in [37] for similar crossing geometries. When voided sleepers in the crossing panel are considered, see Fig. 27, a maximum sleeper displacement of 3.0 mm is observed for the case with no ballast contact for three consecutive sleepers. If only one sleeper is voided, the maximum sleeper displacement is similar to a case where the void under three consecutive sleepers is limited to 1 mm. As expected, changes in ballast stiffness, and especially the presence of voided sleepers, have a significant influence on maximum sleeper displacement. However, it would be difficult to detect a single voided sleeper from reconstructed sleeper displacement data unless the full sleeper displacement signature is accounted for. For reference, a sleeper displacement magnitude of 3 mm is often used by infrastructure managers as a limit where maintenance needs to be performed. Here the simulations show that the influence of the ballast properties on the vertical wheel–rail contact force is relatively insignificant.

In Fig. 28 and Fig. 29, results are presented for the cases with the scanned crossing geometries A and B of Fig. 5 and Fig. 6. The influence of rail pad stiffness and direct fixing design is illustrated in Fig. 28. For crossing A, the direct fixing leads to a 22 kN increase in the maximum wheel–rail contact force and a 0.11 mm increase in maximum sleeper displacement relative to the case with a soft rail pad. Compared to the baseline simulation case with a nominal crossing geometry, see input data in Table 4, the measured crossing geometry A leads to a 25 kN increase in maximum contact force and a 0.02 mm increase in maximum sleeper displacement for the same track properties. This indicates that it would be difficult to detect small crossing rail geometry changes (crossing geometry A is in good condition and close to the nominal design) from reconstructed sleeper displacements. Also, the small variation in results for different rail pad stiffnesses indicates that it would be difficult to detect changes in the rail fastening system from reconstructed sleeper displacements.

According to the 3D scan shown in Fig. 5, crossing geometry B has been subjected to more degradation leading to a greater dip in the wheel–rail vertical trajectory, see Fig. 29(b). For this crossing geometry, the corresponding increases in maximum wheel–rail contact force and maximum sleeper displacement are 54 kN and 0.05 mm when comparing the soft rail pad with the direct fixing. By comparing the results for crossing geometry B (nominal track parameters according to Table 4) with the nominal crossing geometry, a large increase in contact force is observed, 64 kN, but a moderate increase in sleeper displacement, 0.09 mm (12.5%). Considering the variability in reconstructed displacements magnitudes, see Figs. 17 to 20, such a moderate change in sleeper displacement signature would be difficult to identify as a degraded crossing geometry state.

For the displacement bandpass filtered RMS quantity introduced in Fig. 23, a small influence of rail pad stiffness on sleeper displacement is observed in Fig. 28 and Fig. 29. However, when comparing the RMS of the bandpass-filtered displacement between the two scanned crossing rail geometries, a significant difference is observed. It is about 78% higher for crossing B compared to crossing A. This observation indicates that a target bandpass filtering of the displacement signal shows potential for diagnosing crossing geometry status. This quantity has been further investigated in Milosevic et al. [36] where it is shown that there is a strong correlation between the magnitude of these irregularities and the dynamic impact force on the crossing in a frequency range of up to 250 Hz. The RMS of this band-pass filtered displacement is therefore correlated to the shape of the global crossing geometry associated with the so-called P2 force where the wheel is oscillating in phase with the track geometry, while it cannot observe short wavelength rail defects in the frequency range of the P1-force at 500–1000 Hz [36].

To summarise, for the parameters investigated in this study, the crossing geometry changes caused the highest increase in wheel–rail contact forces and track response.

7. Conclusions

This paper has addressed key method developments for online condition monitoring of crossing panels. The focus of the work has been guided by two identified gaps in the literature on S&C condition monitoring: The lack of a methodology that 1) specifically addresses the signal processing aspect of S&C condition monitoring, and 2) sets S&C operational condition monitoring evaluations in the perspective of the railway network with a demonstration of possibilities for a robust large scale processing of measurement data.

The analysis was performed based on sleeper acceleration measurement data generated by 100 000 train passages in eight crossing panels. Based on the given data, a novel frequency-domain displacement reconstruction method was developed and the robustness of the method with respect to encountered operational variability of the measured data was accomplished. To identify train types and obtain better information about the operational loading in the condition monitoring data, a train type and speed identification algorithm was developed. The presented condition monitoring framework is completely automatised from the dataset of measured accelerations (Fig. 3) to the final post-processed long-term results shown in Figs. 19 to 22. To aid the interpretation of the measured results, a parameter study based on simulation was performed for the dynamic vehicle–track interaction in the crossing panel.

7.1. Conclusions from the data analysis

From the processing of acceleration data, it was demonstrated that reconstructed sleeper displacements show variability between train passages and over time for each crossing panel. Nevertheless, each crossing panel demonstrated a distinct range of sleeper displacement responses over the 110 days of measurements.

In the measurement data, there was a consistent difference between the Höör and Stehag sites where turnouts of new and old designs have been installed, respectively. The new turnouts feature resilient soft rail pads in the fastenings between the crossing rail and sleepers, while the old design has a direct and much stiffer fixing of the crossing rail to the sleepers. As a group, the old design turnouts demonstrated more high-frequency energy in their sleeper response signals and this can be indicated by the sleeper displacement signatures in the spatially band-pass filtered domain of 1–0.1 m wavelengths. Additionally, on average these turnouts also demonstrated higher maximum sleeper displacements indicating a difference in ballast conditions between the sites.

From these observations alone, it is not possible to determine the origins of the difference in the high-frequency signal energy as there are a number of possible confounding differences between the two sites (e.g. differences in ballast conditions, differences in crossing geometry status, etc.). However, based on the influence of both rail pad stiffness and crossing geometry condition on sleeper displacement as demonstrated in the simulations, it is likely that the difference in signal energy observed between the sites is a result of a combination of these features.

7.2. Conclusions for condition monitoring

It has been demonstrated that the presented displacement reconstruction algorithm allows for a robust observation of sleeper displacements. As vertical sleeper displacement is a direct indicator of the stiffness of the sleeper support, the algorithm can be directly applied to observe changes in the support provided by the ballast underneath the crossing transition and indicate any sleeper voids. By observing the variability in maximum sleeper displacements for the whole monitoring period, it is suggested that long-term trends should be observed for maintenance decisions.

As demonstrated in the presented simulations and in previous studies, see e.g. [9,38], the degradation status of the crossing geometry determines the relative kinematic displacement between wheel and rail, which strongly influences the vertical wheel–rail contact force. As this wheel–rail interaction is of higher frequency, the maximum sleeper displacement is not a reliable indicator of changes in the crossing geometry. In this paper, the RMS of sleeper displacement signatures in a spatially band-pass filtered domain was presented as a possible indicator of crossing geometry quality. Here, the wavelength range of 0.1–1.0 m was used. Further work on this indicator has been performed in Milosevic et al. [36] and it is shown that it has a strong correlation to the crossing geometry condition. Overall, the separation of the track response into a quasi-static and a dynamic wavelength domain to observe the ballast condition and the crossing geometry condition, respectively, appears reasonable.

7.3. Implications for instrumentation

In Table 1, it was shown that almost 50% of the train passages in the crossing panels Stehag 21B and 32B did not satisfy the criterion of acceleration magnitude being lower than 50 g. In addition, a minority of signals were dropped due to the lower than 1 g criterion. For the turnout design with a direct fixing of the crossing rail to the sleepers, this concludes that a higher measurement range for accelerations is required. Data was sampled with a 20 kHz rate. Concerning the displacement frequency spectrum, which in this paper is concluded as a quantity of main importance for S&C condition monitoring, this sampling rate is sufficiently high (oversampled). However, to resolve high-frequency measurement noise it is recommended to oversample the measurements and then resample them to lower sampling rates with an anti-aliasing filter. Contrasting accelerometers to other inertial sensors, it was found that geophones might have a cut-off frequency of 4–12 Hz and are limited to a high frequency of 1 kHz [39]. In Minardo et al. [40], the authors used optical sensors to monitor railway traffic achieving a sampling rate for a strain profile of 31.4 Hz. From the analysis and results presented in this paper, it is concluded that those frequency ranges would not be sufficient for resolving S&C sleeper displacements and that the type of accelerometers used to record the data in this study is an appropriate solution for the presented condition monitoring method.

7.4. Future work

Addressing predictive maintenance in condition monitoring opens the opportunity for optimising the economy and reliability of the monitored system. A continuation of the presented work concerns addressing the predictive maintenance with 1) the MBS model that is calibrated from live measurements and simulates damage evolution in operation, and 2) the statistical system based on measurements of monitoring history and calibrated MBS model states history. In conclusion, this work has built a foundation for addressing the mentioned predictions and putting the MBS model development in a digital twin landscape for model-based condition monitoring of S&C crossing panels.

Declaration of Competing Interest

The authors declare that they have no known competing financial interests or personal relationships that could have appeared to influence the work reported in this paper.

Data availability

The authors do not have permission to share data.

Acknowledgements

The current study is part of the ongoing activities in CHARMEC – Chalmers Railway Mechanics (www.chalmers.se/charmec). Parts of the study have been funded within the European Union’s Horizon 2020 research and innovation programme in the project In2Track2 under grant agreement No 826255 and In2Track3 under grant agreement No 101012456. The acceleration data used in this research was acquired with sensors from Konux GmbH and received from Trafikverket (the Swedish Transport Administration).

References

[1] E. Kassa, C. Andersson, J.C. Nielsen, Simulation of dynamic interaction between train and railway turnout, Veh. Syst. Dyn. 44 (2006) 247–258.
[2] I. Grossoni, P. Hughes, Y. Bezin, A. Bevan, J. Jaiswal, Observed failures at railway turnouts: failure analysis, possible causes and links to current and future research, Eng. Fail. Anal. 119 (2021), 104987.
[3] R. Skrypnyk, U. Ossberger, B.A. Pålsson, M. Ekh, J.C.O. Nielsen, Long-term rail profile damage in a railway crossing: field measurements and numerical simulations, Wear 472–473 (2021), 203331.
[4] A. Cornish, Life-time monitoring of in service switches and crossings through field experimentation, Imperial College London, 2014. PhD thesis,.
[5] W.-J. Zwanenburg, Modelling degradation processes of switches & crossings for maintenance & renewal planning on the Swiss railway network, Swiss Federal Institute of Technology Lausanne, 2009. PhD thesis,.
[6] M. Sysyn, O. Nabochenko, V. Kovalchuk, Experimental investigation of the dynamic behavior of railway track with sleeper voids, Railway Eng. Sci. 28 (2020) 290–304.
[7] T. Dahlberg, M. Ekh, J. Nielsen, State-of-the-art study on railway turnouts: dynamics and damage, Chalmers tekniska högskola (2004).
[8] L. Le Pen, D. Milne, D. Thompson, W. Powrie, Evaluating railway track support stiffness from trackside measurements in the absence of wheel load data, Can. Geotech. J. 53 (2016) 1156–1166.
[9] P. Torstensson, G. Squicciarini, M. Krüger, B.A. Pålsson, J.C.O. Nielsen, D.J. Thompson, Wheel–rail impact loads and noise generated at railway crossings–influence of vehicle speed and crossing dip angle, J. Sound Vib. 456 (2019) 119–136.
[10] In2Track, Deliverable 2.2, Enhanced S&C Whole System Analysis, Design and Virtual Validation (final), Chapter 3, (2019).
[11] X. Liu, V.L. Markine, Train hunting related fast degradation of a railway crossing—Condition monitoring and numerical verification, Sensors 20 (2020) 2278.
[12] S. Bruni, I. Anastasopoulos, S. Alfi, A. Van Leuven, G. Gazetas, Effects of train impacts on urban turnouts: modelling and validation through measurements, J. Sound Vib. 324 (2009) 666–689.
[13] M.D.G. Milosevic, Towards Model-Based Condition Monitoring of Railway Switches and Crossings, Licentiate Thesis, Chalmers Tekniska Hogskola, Sweden, 2021.
[14] D.J. Rixen, A dual Craig-Bampton method for dynamic substructuring, J. Comput. Appl. Math. 168 (2004) 383–391.
[15] N. Pillai, J.-Y. Shih, C. Roberts, Evaluation of numerical simulation approaches for simulating train-track interactions and predicting rail damage in railway switches and crossings (S&Cs), Infrastructures 6 (2021) 63.
[16] S. Iwnicki, Manchester benchmarks for rail vehicle simulation, Veh. Syst. Dyn. 30 (1998) 295–313.
[17] Y.P. Bezin, Björn A., Multibody simulation benchmark for dynamic vehicle-track interaction in switches and crossings: Modelling description and simulation tasks. v3, University of Huddersfield https://doi.org/10.34696/s60x-ay18, (2019).
[18] J.J. Kalker, A fast algorithm for the simplified theory of rolling contact, Veh. Syst. Dyn. 11 (1982) 1–13.
[19] D. Milne, A. Masoudi, E. Ferro, G. Watson, L. Le Pen, An analysis of railway track behaviour based on distributed optical fibre acoustic sensing, Mech. Syst. Sig. Process. 142 (2020) 106769.
[20] D. Arias-Lara, J. De-la-Colina, Assessment of methodologies to estimate displacements from measured acceleration records, Measurement: Journal of the International Measurement Confederation 114 (2018) 261–273.
[21] F. Lamas-Lopez, Y.J. Cui, S.C. D`Aguiar, N. Calon, Assessment of integration method for displacement determination using field accelerometer and geophone data, J. Zhejiang Univ.-Sci. A 18 (2017) 553–566.
[22] L. Le Pen, G. Watson, W. Powrie, G. Yeo, P. Weston, C. Roberts, The behaviour of railway level crossings: Insights through field monitoring, Transp. Geotech. 1 (4) (2014) 201–213.
[23] D. Milne, L.L. Pen, D. Thompson, W. Powrie, Automated processing of railway track deflection signals obtained from velocity and acceleration measurements, Proc. Inst. Mech. Eng., Part F: J. Rail Rapid Transit 232 (8) (2018) 2097–2110.
[24] D. Bowness, A.C. Lock, W. Powrie, J.A. Priest, D.J. Richards, Monitoring the dynamic displacements of railway track, Proc. Inst. Mech. Eng., Part F: J. Rail Rapid Transit 221 (1) (2007) 13–22.
[25] E. Yazawa, K. Takeshita, Development of measurement device of track irregularity using inertial Mid-chord offset method, Quart. Rep. RTRI 43 (2002) 125–130.
[26] J.S. Lee, S. Choi, S.S. Kim, C. Park, Estimation of Rail Irregularity by Axle-Box Accelerometers on a High-Speed Train, Springer Japan, Tokyo, 2012, pp. 571–578.
[27] M.D. Trifunac, V. Lee, Automatic digitization and processing of accelerograms using PC, University of Southern California Faculty Research and Publications, 90-03, (1990).
[28] A. Converse, A.G. Brady, BAP basic strong-motion accelerogram processing soft- ware version 1.0, United States department of the interior, U.S. Geological survey; distributed by books and open-file reports section, USGS Numbered Series 92–296–A, (1992).
[29] H.-C. Chiu, Stable baseline correction of digital strong-motion data, Bull. Seismol. Soc. Am. 87 (1997) 932–944.
[30] M. Milošević, B. Pålsson, A. Nissen, H. Johansson, J. Nielsen, On tailored signal processing tools for operational condition monitoring of railway switches and crossings, Proceedings of the International Conference on Noise and Vibration Engineering, Leuven (Belgium), (2020).
[31] M. Boogaard, Z. Li, R. Dollevoet, In situ measurements of the crossing vibrations of a railway turnout, Measurement 125 (2018) 313–324.
[32] D. Barke, W.K. Chiu, Structural health monitoring in the railway industry: a review, Struct. Health Monit. 4 (2005) 81–93.
[33] A. Brandt, R. Brincker, Integrating time signals in frequency domain - Comparison with time domain integration, Measurement: Journal of the International Measurement Confederation 58 (2014) 511–519.
[34] E. Berlin, K. Van Laerhoven, Sensor networks for railway monitoring: Detecting trains from their distributed vibration footprints, in: 2013 IEEE International Conference on Distributed Computing in Sensor Systems, IEEE, 2013, pp. 80–87.
[35] R. Krč, J. Podroužek, M. Kratochvílová, I. Vukušič, O. Plášek, Neural network-based train identification in railway switches and crossings using accelerometer data, J. Adv. Transp. 2020 (2020).
[36] M.D.G. Milosevic, B.A. Pålsson, A. Nissen, J.C.O. Nielsen, H. Johansson, Condition monitoring of railway crossing geometry via measured and simulated track responses, Sensors, 22 (2022) 1012, 1010.3390/s22031012.
[37] B.A. Pålsson, J.C.O. Nielsen, Dynamic vehicle–track interaction in switches and crossings and the influence of rail pad stiffness – field measurements and validation of a simulation model, Veh. Syst. Dyn. 53 (2015) 734–755.
[38] In2Rail, Deliverable 2.4, Embeded & integrated sensors: System design selection, 2018.
[39] G. Kouroussis, C. Caucheteur, D. Kinet, G. Alexandrou, O. Verlinden, V. Moeyaert, Review of trackside monitoring solutions: from strain gages to optical fibre sensors, Sensors (Switzerland) 15 (2015) 20115–20139.
[40] A. Minardo, G. Porcaro, D. Giannetta, R. Bernini, L. Zeni, Real-time monitoring of railway traffic using slope-assisted Brillouin distributed sensors, Appl. Opt. 52 (2013) 3770–3776.